Near-surface dynamics of a separated jet in the Coastal Transition Zone off Oregon

A. O. Koch, A. L. Kurapov, J. S. Allen

College of Oceanic and Atmospheric Sciences,

Oregon State University, Corvallis, OR, 97331

akoch@coas.oregonstate.edu

Submitted to the Journal of Geophysical Research

August 8, 2009

Abstract

Three-dimensional circulation in the coastal transition zone (CTZ) off Oregon is studied using a 3-km resolution model based on the Regional Ocean Modeling System (ROMS). The study period is spring-summer 2002, when extensive observations are available from the North Eastern Pacific Component of the Global Ocean Ecosystems Dynamics (GLOBEC-NEP) project. Our main focus is on near-surface transports, particularly in an area off Cape Blanco where an energetic coastal current is separated in the CTZ. Comparisons with available observations (velocities from mid-shelf moorings, surface velocities from high-frequency radars, satellite SST maps, along-track SSH altimetry, and SeaSoar hydrography) show that the model reproduces qualitatively correctly the flow structure and variability in the study area. The near-surface flow behavior during 26 July–21 August, a late-summer time period of strong, time-variable southward winds, is examined. During that period the coastal jet has separated from the continental shelf around Cape Blanco (43 °N). The energetic separated jet continues to flow southward in a near-coastal

Report Documentation Page

Form Approved
OMB No. 0704-0188

1. REPORT DATE
08 AUG 2009

2. REPORT TYPE

3. DATES COVERED
00-00-2009 to 00-00-2009

4. TITLE AND SUBTITLE
Near-surface dynamics of a separated jet in the Coastal Transition Zone off Oregon

5a. CONTRACT NUMBER

5b. GRANT NUMBER

5c. PROGRAM ELEMENT NUMBER

6. AUTHOR(S)

5d. PROJECT NUMBER

5e. TASK NUMBER

5f. WORK UNIT NUMBER

7. PERFORMING ORGANIZATION NAME(S) AND ADDRESS(ES)
Oregon State University,College of Oceanic and Atmospheric Sciences,Corvallis,OR,97331

8. PERFORMING ORGANIZATION REPORT NUMBER

9. SPONSORING/MONITORING AGENCY NAME(S) AND ADDRESS(ES)

10. SPONSOR/MONITOR’S ACRONYM(S)

11. SPONSOR/MONITOR’S REPORT NUMBER(S)

12. DISTRIBUTION/AVAILABILITY STATEMENT
Approved for public release; distribution unlimited

13. SUPPLEMENTARY NOTES

14. ABSTRACT
Three-dimensional circulation in the coastal transition zone (CTZ) off Oregon is studied using a 3-km resolution model based on the Regional Ocean Modeling System (ROMS). The study period is spring-summer 2002, when extensive observations are available from the North Eastern Pacific Component of the Global Ocean Ecosystems Dynamics (GLOBEC-NEP) project. Our main focus is on near-surface transports, particularly in an area off Cape Blanco where an energetic coastal current is separated in the CTZ. Comparisons with available observations (velocities from mid-shelf moorings, surface velocities from high-frequency radars, satellite SST maps, along-track SSH altimetry, and SeaSoar hydrography) show that the model reproduces qualitatively correctly the flow structure and variability in the study area. The near-surface flow behavior during 26 July?21 August, a late-summer time period of strong, time-variable southward winds, is examined. During that period the coastal jet has separated from the continental shelf around Cape Blanco (43 ◦N). The energetic separated jet continues to flow southward in a near-coastal region between 42:2 ◦N and 43 ◦N. It subsequently turns around 42 ◦N to flow westward offshore past 127 ◦W. Relatively vigorous upwelling and downwelling is found concentrated in the region of the separated jet. Frontogenesis secondary circulation nonlinear effects of the relative vorticity on the ageostrophic Ekman transport, and submesoscale instabilities contribute to the vertical circulation within the jet. Vertical velocities are found to reach 50 m day−1 in the offshore part of the jet and 100 m day−1 in the near-coastal part, where the jet is aligned with the wind direction.

15. SUBJECT TERMS

16. SECURITY CLASSIFICATION OF:			17. LIMITATION OF ABSTRACT	18. NUMBER OF PAGES	19a. NAME OF RESPONSIBLE PERSON
a. REPORT **unclassified**	b. ABSTRACT **unclassified**	c. THIS PAGE **unclassified**	**Same as Report (SAR)**	**61**	

region between 42.2 °N and 43 °N. It subsequently turns around 42 °N to flow westward offshore past 127 °W. Relatively vigorous upwelling and downwelling is found concentrated in the region of the separated jet. Frontogenesis secondary circulation, nonlinear effects of the relative vorticity on the ageostrophic Ekman transport, and submesoscale instabilities contribute to the vertical circulation within the jet. Vertical velocities are found to reach 50 m day^{-1} in the offshore part of the jet and 100 m day^{-1} in the near-coastal part, where the jet is aligned with the wind direction.

1 Introduction

The coastal transition zone (CTZ) is a region of open ocean adjacent to the continental shelf where dynamics are affected by shelf processes. During periods of summer upwelling off the U.S. west coast, narrow filaments of cold water are separated from the shelf to the CTZ [*Brink and Cowles*, 1991]. For instance, off Oregon, a distinctive offshore feature in late summer is a coastal jet separated near Cape Blanco (42.8 °N) [*Barth et al.*, 2000]. This jet may reach a speed of 0.8 m s^{-1} at the surface [*Strub et al.*, 1991] and carry cold and nutrient-rich coastal waters as far as 200 km offshore, enhancing dynamic and biological variability in the CTZ. This prominent feature is clearly seen in satellite SST imagery (Figure 1).

The separated coastal jet is associated with various dynamical processes: frontogenesis, nonlinear jet-wind interaction, disturbances and instabilities of different nature and scale. The objective of the present study is to investigate the near-surface structure and dynamics of the coastal upwelling jet separated off the Oregon coast by the means of numerical simulations and dynamical analysis.

Despite a number of studies that discuss possible mechanisms for coastal current separation off Cape Blanco, to this day there is not a settled opinion on the dominant dynamical processes. Contributing factors may include interactions with topography [*Castelao and Barth*, 2007], enhanced wind stress south of Cape Blanco [*Samelson et al.*, 2002],

interactions of the coastal current with the southward undercurrent [*Barth et al.*, 2000], and alongshore pressure gradients set up during periods of relaxation from upwelling [*Gan and Allen*, 2002].

Shelf processes are relatively better studied than those in the CTZ, owing in large part to the success of recent coordinated observational and modeling programs, e.g., Coastal Ocean Advances in Shelf Transport [COAST, *Barth and Wheeler*, 2005 and other papers in that special issue]. Advances in satellite oceanography have influenced progress in understanding near-surface transports in the CTZ. However, observations of the three-dimensional (3D) structure of jets, eddies and filaments in the CTZ have been limited. One of the most coordinated efforts in that regard was the CTZ program of 1986–87 [see *Brink and Cowles*, 1991, and other papers in that special issue]. *Kadko et al.* [1991] and *Washburn et al.* [1991] reported significant vertical transport of upwelled water within the jets as they propagate offshore. *Washburn et al.* [1991] analyzed phytoplankton data to track coastal water that moves offshore and found that the near-surface water can subduct to a depth of 100 m within the jet core. The associated estimated vertical speed reached 6–10 m d^{-1}. *Dewey et al.* [1991] explored the structure and dynamics of a coastal upwelling jet separated off Point Arena, California based on observations made over a two week period during sustained southward wind. They found asymmetry in the cross-jet relative vorticity and evidence for downwelling and upwelling within the jet. The estimated maximum vertical velocities reached 40 m d^{-1} and were thought to be associated with the observed asymmetry in the relative vorticity field.

Numerical modeling studies focused on California-Oregon shelf flows [e.g., *Gan and Allen*, 2002; *Castelao and Barth*, 2007] do not always correctly reproduce the westward extent of separation in the CTZ, potentially due to a limited domain size, and idealized boundary conditions and wind stress. However, jets extending off main topographic coastal features were obtained in multi-year simulations using a regional scale 5-km resolution model of the U.S. west coast run with seasonally-varying atmospheric forcing

[*Marchesiello et al.*, 2003]. *Springer et al.* [2009] developed a 3-km resolution model based on the Regional Ocean Modeling System (ROMS) with realistic atmospheric forcing and boundary conditions provided by the Naval Coastal Ocean Model–California Current System (NCOM-CCS) [*Shulman et al.*, 2004]. The 3-km ROMS model reproduces coastal jet separation off Cape Blanco qualitatively correctly. That study focused more on shelf processes, and did not examine dynamical processes in the CTZ, in particular, the jet structure. In this paper, we utilize a similar model configuration to simulate flows in summer 2002, when extensive observations from the Global Ocean Ecosystems Dynamics in the North-East Pacific (GLOBEC-NEP) field program [*Strub et al.*, 2002] are available. We use that data to evaluate model performance. Then, we analyze the structure of the jet separated off Cape Blanco with an emphasis on near-surface behavior, particularly under strong wind conditions.

2 Model

Our model is based on ROMS, which is a free-surface, terrain-following, primitive equation ocean model widely used by the scientific community for various applications [e.g., *Haidvogel et al.*, 2000; *Marchesiello et al.*, 2003; *Di Lorenzo*, 2003]. Algorithms that comprise a ROMS computational kernel are described in detail by *Shchepetkin and McWilliams* [2003, 2005].

The model computational domain, shown in Figure 1, extends from 40.5 °N to 47.5 °N in the meridional direction and from the coast, near 124 °W, offshore to 129 °W. The grid has approximately 3 km horizontal resolution and 40 terrain-following layers in the vertical with a relatively better resolution near surface and bottom. Bottom topography is composed by merging two sets: a high resolution (12”) NOAA-NGDC Bathymetry of the U.S. west coast, representing features on the shelf and continental slope, and a lower resolution (5’) ETOPO5 product [*NGDC*, 1988]. A minimum depth of 10 m is set along the coastline.

The study period is from 1 April to 31 August 2002. Initial and boundary conditions are obtained from the 9 km horizontal resolution NCOM-CCS model [*Shulman et al.*, 2004] that spans between (134.5 °W, 116 °W) and (30 °N, 48.5 °N). The NCOM-CCS solution was constrained by assimilation of SSH and SST using a nudging approach [*Shulman et al.*, 2004, 2007]. At the open boundaries of our model, the free surface elevation, barotropic and baroclinic velocities, water temperature and salinity are provided daily. Radiation conditions in combination with a relaxation nudging term are applied for baroclinic velocities and for temperature and salinity at open boundaries [*Marchesiello et al.*, 2001]. Flather conditions [*Flather*, 1976] are utilized for the normal barotropic velocities, and Chapman conditions for the free surface [*Chapman*, 1985].

To force our model, we calculate surface wind stress from the same time- and space-dependent surface wind velocity fields that were originally used to force NCOM-CCS, provided from the Coupled Ocean/Atmosphere Mesoscale Prediction System (COAMPS) [*Hodur*, 1997] with 9 km horizontal and daily temporal resolution. Other atmospheric variables (air temperature, pressure, relative humidity, precipitation, and solar short-wave radiation), used to compute atmospheric fluxes based on bulk flux parameterizations [*Fairall et al.*, 2003], are obtained from the National Center of Environmental Prediction (NCEP) reanalysis [*Kalnay et al.*, 1996] and are provided as monthly fields, describing seasonal variability. Figure 2 shows time series of the wind stress at two mid-shelf locations within the model domain, near Newport (44.6 °N) and the Rogue River (42.4 °N), projected onto their respective major principal axes, which are approximately aligned with the coast. During spring-summer the wind stress over the Oregon shelf is predominantly southward with rare and short events of northward, downwelling favorable winds. The wind stress is substantially larger south of Cape Blanco [*Samelson et al.*, 2002].

The effects of vertical turbulence are calculated using the *Mellor and Yamada* [1982] 2.5-level turbulence closure scheme, modified by *Galperin et al.* [1988]. Horizontal turbulence is parametrized using a harmonic term with eddy diffusivity and viscosity coefficients

of 10 m^2 s^{-1}. To minimize effects of reflection at the boundaries, a sponge layer is introduced in an area of width 120 km along the open boundaries, in which horizontal dissipation is gradually increased to 30 m^2 s^{-1} toward the edges of the domain.

3 Model-data comparisons

3.1 SST

A comparison of the model monthly-averaged SST with 5-km horizontal resolution monthly SST composites from the Geostationary Operational Environmental Satellite [GOES, *Maturi et al.*, 2008] has shown that the model simulates the seasonal development of the surface temperature field qualitatively correctly (Figure 1). In the plots of the satellite measurements for June and July, patches of cooler temperature can be associated with clouds. The extent of the temperature front off Cape Blanco, particularly apparent in July and August, is similar in the model and in the satellite imagery. The features of the temperature front in the monthly means are sharper in the model plots than in the satellite plots. We hypothesize that small scale horizontal eddy fluxes, unresolved in our model, could contribute to smearing the monthly mean observed fronts, and to increased temporal variability of the jet position.

3.2 ADCP velocities

Continuous time series of Acoustic Doppler Current Profiler (ADCP) velocities were measured in 2002 at three mid-shelf moorings: NH10, 44.6 °N, in water depth H=81 m [*Kosro*, 2003], Coos Bay, 43.2 °N, H=100 m [*Hickey et al.*, 2009], and Rogue River, 42.4 °N, H=76 m [*Ramp and Bahr*, 2008]. Mooring locations are shown in Figure 1. Figure 2 shows time series of 40-hour low-pass filtered depth-averaged velocities at the mooring locations, model and observations, projected onto their respective major principal axes that deviate slightly from the meridional direction. At each mooring, the model-data correlation co-

efficient (CC) is high (>0.68), and the root mean square error (RMSE) is low (<0.14 m s^{-1}). At the Rogue River mooring, south of Cape Blanco, the observations show increased variability on the temporal scale of several days not well described by the model (see Figure 2e). This variability correlates with that in the wind stress (Figure 2b). The reason for this strong response to the wind in this frequency band is not entirely understood. However, we speculate that part of that response may be due to remote forcing south of our domain that is not totally represented by the southern boundary conditions. Figure 3 shows time-averaged means and variance ellipses for the depth-averaged currents at the mooring locations. Both the data and model reveal larger current variability in the alongshore direction. The magnitude and direction of the mean current and the variance are very similar in data and model. Curiously, the mean current at the Rogue River site inside the separation zone south of Cape Blanco is close to 0, despite large and predominantly southward wind stress at that location.

Time-averaged statistics of the measured currents from the three moorings are compared with corresponding model currents as a function of depth in Figure 4. Fairly good agreement of the observed and modeled mean values and standard deviations for both the larger alongshore v and smaller cross-shore u components is found at NH10 and Coos Bay. At Rogue River, the signs of the observed and modeled mean v differ below 25 m, but both are relatively small. The standard deviations at Rogue River are similar in magnitude to those at NH10 and Coos Bay with observed values slightly larger. At all of the moorings, the correlations of the observed and modeled along-shore velocity v are reasonably high while those of the cross-shore velocity u are considerably lower. Likewise, the normalized root mean square errors (NRMSE) are substantially lower for v than for u. The greater success in modeling the fluctuations in the larger along-shore currents v compared with the smaller cross-shore currents u is consistent with previous model results for mid-shelf currents off Oregon [e.g. *Springer et al.*, 2009].

3.3 HF-radar currents

To assess the accuracy of model surface currents in the area around Cape Blanco, we compare the model and maps derived from long-range HF radars [*Paduan et al.*, 2004; *Kosro*, 2005]. HF radar locations are shown in Figure 1. The radial velocity components with 6 km along-beam resolution were low-pass filtered, recomputed into zonal and meridional components, daily averaged and mapped on a 6 km regular grid by P.M. Kosro (OSU). Figure 5 shows observed and model monthly averaged surface current, speed, and the RMS speed of deviations from the mean, defined as

$$U_{RMS} = \left[\overline{(u-\bar{u})^2 + (v-\bar{v})^2}\right]^{\frac{1}{2}} \quad , \tag{1}$$

where the over-bar denotes a time-average.

The model and observed current patterns are qualitatively comparable. In May the surface jet is already separated from the Cape and flows southward. By July, the observed currents form two jets, one south and one north of Cape Blanco. A similar structure is seen in the model, although it appears earlier in June. The observed jets are wider and less energetic than modeled. This may come partly from the smoothing effect of the mapping procedure performed on the radial data and/or from small scale eddy variability unresolved in the model. By August, when the model jet turns westward at 42 °N, the data show a similar westward orientation of the flow, although the observed monthly mean is diffused over a larger area. The magnitude of the monthly averaged model current within the jets is similar to observed magnitudes in May–June (0.3–0.5 m s^{-1}), and is 30–40 % higher in the model (0.6–0.7 m s^{-1}) than in the observations (0.2–0.5 m s^{-1}) in July–August. The variability of the current, showed by U_{RMS} (Figure 5), is of the same order (0.1–0.25 m s^{-1}) in the observations and the model in May–July, with increased variability found over the shelf and in the CTZ jets. Although variability in the HF-radar data in August (0.1–0.2 m s^{-1}) is lower than in the model (0.02–0.3 m s^{-1}), it

is distributed more evenly over the area. This, together with the fact that the observed mean currents are more spatially uniform than the modeled currents, suggests that the position of the observed separated jet fluctuates over the domain more than that of the modeled jet. Again, we speculate that eddy variability on scales <10 km, not represented in our model, contributes to jet instability and variability.

Despite the fact that the jet is not seen clearly in monthly averaged observed fields in August, it may be readily identified in daily plots (Figure 6). The dates in Figure 6 are chosen so that satellite SSH observations are available along the track that passes through the area (shown as the white line, see discussion in Section 3.4). The model and observed jets in the daily plots (Figure 6) are found to have comparable speeds (0.6–0.8 m s^{-1}), and across-jet spatial scales (10–30 km).

3.4 SSH

In summer 2002, the AVISO (Analysis, Validation and Investigation of Satellite Oceanography, www.aviso.oceanobs.com) satellite SSH altimetry (sea level anomaly) is available along the orbits of the TOPEX/Poseidon satellite with 10 day periodicity [*Fu et al.*, 1994]. Six tracks cross our model domain area. Here we show comparison with the data from track 206, which passes through the area covered by the HF radar (see Figure 6). For this analysis, along-track means are taken out from both the model and observational lines. Variability in SSH is of similar magnitude and horizontal scale in both the satellite data and the model and can be associated with jets and eddies in the CTZ. The SSH gradient is proportional to the surface geostrophic current normal to the track. Using the satellite data, the estimated geostrophic current in the jets can be as large as 0.6–0.8 m s^{-1}. However, the location and intensity of individual jets and eddies in the along-track data and model do not necessarily coincide. It is possible that assimilation of SSH data in a model of this class can improve the representation of the time-dependent eddy dominated flows in the CTZ.

3.5 Density

In the beginning of August 2002, vertical cross-shore sections of potential density σ_θ were measured as part of a SeaSoar survey [*O'Malley et al.*, 2002; *Barth et al.*, 2005]. The comparisons of three cross-shore density sections measured along 41.9 °N, 43.5 °N, 44.25 °N in the beginning of August with sections sampled at the same times and locations from the model results are presented in Figure 7. There is a qualitative and quantitative agreement between data and model in the two sections north of Cape Blanco (Figure 7a–d), especially in the shape, slope and spacing of the isopycnals that provide information on properties of the upwelling density front, and the associated normal geostrophic flow. The model-data agreement in the southernmost section is not as close. In particular, the eddy shown by the uplift of isopycnals near 125.3 °W (Figure 7e) is only weakly represented in the model section (Figure 7f). This behavior reflects the difficulty, found also in Section 3.4 in connection with model/data SSH comparisons, of deterministically modeling the individual filaments and eddies in the energetic separated flow region offshore south of Cape Blanco.

4 Dynamical analyses of jet structure

4.1 Mean near-surface circulation

In order to explore the mean near-surface circulation in the CTZ off Oregon, we choose a late summer 27 day time interval from 26 July to 21 August when the wind over the study area is generally upwelling-favorable, but varies in time on a typical several-day time scale (Figure 8) and the separated jet is well developed and extends offshore as far as 200 km (Figure 9). The region of relatively large horizontal gradient of the time-mean surface density field, along with the SSH field, shows the upwelling front location (Figure 9, left). The coastal upwelling jet is rather discontinuous along the front and breaks into a few separation zones. The separated jet intensifies and reaches maximum values of

0.6–0.7 m s^{-1} south of Cape Blanco (Figure 9, right). The maximum jet variability is found within these separation zones. North of the Heceta Bank complex, around 45 °N, the separated jet has approximately equal strengths in its along- and normal to coast components. In contrast, offshore in the separation zone south of Cape Blanco the jet is noticeably stronger than its upstream along-coast link, whose strength may be weakened by the cyclonic mesoscale eddy, located west of the jet and centered near 43 °N, 125.7 °W, that is stationary through the averaging interval.

Horizontal fields of the mean and standard deviation of the vertical velocity at 25 m depth over this time period (Figure 10) show interesting behavior. In particular, the spatial pattern of the standard deviations of w, which can reach magnitudes typically two times greater (around 20 m day^{-1}) than the magnitudes of the mean values (around 10 m day^{-1}) show relatively large values strongly concentrated in the region of the separated jet. That region extends along the jet from a location within about 60 km of the coast near Cape Blanco (43 °N), where the separating jet is directed southward, offshore to about 127 °W, where the jet is flowing westward. The magnitude of the mean values of w (Figure 10) are appreciable in a similar spatial region, but with greater values in the near-coastal location between 42.2 °N and 43 °N, where the jet flows southward. The behavior in that location is characterized by concentrated mean upwelling velocities offshore in the jet, with downwelling velocities immediately inshore.

The horizontal spatial structure of the mean and standard deviation of the vertical velocity at 25 m depth in Figure 10 is remarkable. In particular, it reflects the presence of energetic near-surface ageostrophic processes that are relatively localized in the vicinity of the separated coastal jet off Cape Blanco. It also provides motivation for the analyses that follows of the time-dependent dynamics that leads to the large variability in near-surface vertical velocities in this region.

4.2 Lagrangian analysis of surface flows

To get an idea of the general character of Lagrangian flows in the CTZ during the chosen late summer time period, we release 65 model surface particles simultaneously on 1 August-0000 (UTC, hereinafter) along the 81 m isobath (the depth of mooring NH10) every 10 km in the meridional direction between latitudes 41 °N and 47 °N. Model trajectories are obtained by integration of surface velocities, saved every 4 hours, using a 4th order Runge-Kutta method. The particles, advected by the surface current, begin to group in offshore directed filaments over the initial period 1–10 August (Figure 11). The speed of the particles entrained in filaments can be several times higher than the speed associated with the offshore Ekman transport. For the trajectories over 1–20 August (Figure 11) we can see two major compact jets that originate, respectively, over the shelf near the Heceta Bank complex (44 °N) and near Cape Blanco (43 °N). The pattern of surface trajectories over the Oregon CTZ (Figure 11) is qualitatively consistent with the shape of the observed SST front in August (Figure 1).

4.3 Surface strain rate field

Although Lagrangian tracking described above is a powerful visualization tool, it is limited to areas where particles are seeded at an initial time or found later. To quantify the rate of relative surface particle separation over the entire domain, the surface strain rate tensor can be computed:

$$\begin{bmatrix} \varepsilon_{xx} & \varepsilon_{xy} \\ \varepsilon_{yx} & \varepsilon_{yy} \end{bmatrix} = \begin{bmatrix} \dfrac{\partial u}{\partial x} & \dfrac{1}{2}\left(\dfrac{\partial u}{\partial y} + \dfrac{\partial v}{\partial x}\right) \\ \dfrac{1}{2}\left(\dfrac{\partial u}{\partial y} + \dfrac{\partial v}{\partial x}\right) & \dfrac{\partial v}{\partial y} \end{bmatrix}, \tag{2}$$

where (x, y) are local Cartesian coordinates [e.g., *Batchelor*, 1967, Section 2.3]. The di-

agonal elements of the matrix, ε_{xx} and ε_{yy}, represent the normal strain rate and the non-diagonal elements, $\varepsilon_{yx} = \varepsilon_{xy}$, the shear strain rate. At each location, the strain rate tensor can be rotated to principal axes, in which the shear component is zero and the normal components ε_1 and ε_2 are:

$$\varepsilon_{1,2} = \overbrace{\frac{1}{2}(\varepsilon_{xx} + \varepsilon_{yy})}^{\text{divergence term}} \pm \overbrace{\left[\frac{1}{4}(\varepsilon_{xx} - \varepsilon_{yy})^2 + \varepsilon_{xy}^2\right]^{\frac{1}{2}}}^{\text{deformation term}} . \tag{3}$$

The first term on the right hand side of (3) is the divergent component. It provides an estimate of the relative particle separation rate due to the relative change of the surface area. The second, deformation component quantifies the particle separation rate due to the change in the shape of a small surface domain, without changes of its area.

Figure 12 shows the two terms in the principal surface strain rate field (3), averaged over the 27 day period, 26 July–21 August. In these averaged maps the deformation part of the principal strain rate is dominant. Note that there is divergence in the surface current near the coast associated with surface Ekman transport, although in the monthly averaged plot its magnitude is smaller than that of the deformation part of the strain rate. In the following we will examine the flow during the wind event around 1 August. On this date, offshore between 125 °W and 127 °W, an energetic separated jet is directed westward approximately along 42 °N (Figure 13, right). The wind stress in the area of the jet is strong (-0.35 N m^{-2}) (Figure 8) and is directed southward, nearly perpendicular to the jet direction (Figure 13, left). Velocities within the jet reach 0.9 m s^{-1}. During this event the divergence term of the principal strain rate becomes comparable in magnitude to the deformation term, particularly along the paths of the CTZ jets (Figure 12c,d). Both terms are increased in magnitude compared to the 27 day averages (note that color bar limits for Figure 12a,b and Figure 12c,d are different). Since the divergence of the surface horizontal flow is entirely due to its ageostrophic component, i.e. $\nabla_h \cdot \mathbf{u} = \partial u_a/\partial x + \partial v_a/\partial y$

(Section 4.4), this analysis provides an additional indication of the important role of time-dependent ageostrophic processes in the near-surface dynamics of the separated jet south of Cape Blanco.

4.4 Structure of the separated jet on 1 August

To study further the nature of the flow that leads to the large mean and RMS near-surface vertical velocities in the region of the separated jet (Figure 10) we examine some instantaneous horizontal fields and vertical sections on 1 August, during a period of strong southward winds (Figure 8) when the offshore separated jet is well developed (Figure 13, right). The wind stress field on 1 August (Figure 13, left) shows the known spatial increase in magnitude of the wind stress south of Cape Blanco [*Samelson et al.*, 2002]. It also shows that on 1 August the stress vectors have a predominantly north-south direction in the region of the separated jet ($41.5 - 43\,°\mathrm{N}, 124.5 - 127\,°\mathrm{W}$). We look first at the vertical jet structure along two sections, one near-coastal, east-west section along 42.63 °N and one offshore, north-south section along 126 °W (locations shown in Figure 13). Instantaneous values of potential density σ_θ, the respective geostrophic along-jet velocity components $v_g = (1/f\rho_0)(\partial p/\partial x)$ and $u_g = -(1/f\rho_0)(\partial p/\partial y)$, the ageostrophic $v_a = v - v_g$, $u_a = u - u_g$ velocity components, where f is the Coriolis parameter, ρ_0 is the reference density and p is the pressure, are shown in Figure 14.

At the location of the near-coastal, east-west section, the coastal jet has separated offshore of the continental shelf, but is still flowing southward in the direction of the wind stress (Figure 13). The dominant along-jet v velocities are in geostrophic balance with a density field characterized by a strong upwelling frontal structure (Figure 14). There is some augmentation of the southward geostrophic v_g velocities by an ageostrophic v_a component in the jet core. The across-jet and vertical ageostrophic velocities exhibit characteristics of frontogenesis secondary circulation (FSC) [*Hoskins*, 1982; *Capet et al.*, 2008b]. That circulation is dominated by vigorous downwelling on the inshore, high den-

sity side of the jet, concentrated in a region with small horizontal scale of about 10 km. Correspondingly vigorous upwelling occurs adjacent on the lower density side over a similar short horizontal scale. The vertical scales of the larger downwelling and upwelling velocities extend to about 90 m depth. The near-surface ageostrophic u_a velocity component is primarily negative and directed offshore, presumably driven by the southward wind stress in general accordance with Ekman dynamics. In the vicinity of the front, however, u_a weakens considerably and reverses sign, as it takes part in the vertical circulation processes. The basic characteristics of this wind-intensified FSC are in agreement with that predicted by recent theoretical and modeling studies [e.g., *Thomas and Lee*, 2005]. We note that u_a appears to be larger in magnitude offshore on the negative vorticity side of the jet which would be consistent with the nonlinear effect of the geostrophic relative vorticity $\partial v_g/\partial x$ on the Ekman dynamics [*Stern*, 1965, *Niiler*, 1969, *Thomas and Lee*, 2005], represented as

$$M_E^x = \int_{-\delta_E}^{\eta} u_a \, dz = \frac{\tau^y}{\rho_0(f + \partial v_g/\partial x)}. \tag{4}$$

At the location of the offshore north-south section, the separated jet is flowing westward (Figure 13). During this strong wind event (and during the entire averaging period 26 July–21 August) the separated jet advects cold dense water, upwelled near the coast, westward (Figure 13). By the thermal wind balance, the vertical shear in u_g (Figure 14) is of opposite signs on the two sides of the jet. As a result, the zonal along-jet geostrophic velocity u_g has an asymmetric structure in the across-jet north-south section. The negative along-jet u_g velocities are strengthened in this section by a negative ageostrophic u_a component, which appears to be primarily wind-driven, but is again relatively large locally in the jet core. The ageostrophic v_a component is negative (southward) near the surface and positive at depths greater than about 20 m,with notably larger magnitudes on

the northern, negative vorticity, side of the jet. Energetic vertical circulation is present, involving upwelling concentrated in a small $O(10\ \mathrm{km})$ horizontal scale region on the northern, lower density side of the jet with adjacent downwelling on a similar horizontal scale on the southern, higher density side. This vertical circulation appears to be primarily associated with along-jet submesoscale instabilities (to be discussed in Section 4.5). We note that the structure of the vertical velocity is qualitatively similar to the conceptual picture of vertical processes in an observed CTZ jet based on the analysis of hydrographic data in the CTZ field experiment [*Dewey et al.*, 1991].

To examine other dynamical features associated with the separated jet in these two locations we plot in Figure 15 corresponding across-jet vertical sections of buoyancy frequency $N^2 = -(g/\rho_0)(\partial\sigma_\theta/\partial z)$, turbulent vertical diffusivity coefficient K_h, turbulent kinetic energy (TKE), including contours of the Richardson number $Ri = N^2/S^2$, where $S^2 = (\partial u/\partial z)^2 + (\partial v/\partial z)^2$ is the sum of the squared vertical shear of the horizontal velocity components, and turbulent shear production $P = K_m S^2$, where K_m is the turbulent vertical viscosity coefficient [e.g. *Wijesekera et al.*, 2003]. In both sections, large values of buoyancy frequency (Figure 15a,e) reflect stable vertical stratification and correspond to the areas of relatively large vertical density gradients (Figure 14a,f). Areas of unstable stratification with negative N^2, marked by the white stars, result, through the turbulent closure scheme, in accompanying large values of vertical diffusivity K_h (Figure 15b,f). In the coastal section, the unstable region with large K_h at about 124.9 °W appears to be related to the downwelling circulation at that location, but unstable conditions are found at other locations away from the frontal regions of strong vertical circulation as well. In both sections, regions of relatively large TKE are found in the surface layer on the light side of the front (Figure 15c,g), reflecting the results of relatively large shear production P (Figure 15d,h) in those locations. In the offshore section, the region of large surface layer TKE is considerably greater and extends farther from the jet core. An additional analysis (not shown here) shows that the enhanced shear production in that region is

caused by the shear in the ageostrophic across-jet velocity component v_a.

The sections of TKE and K_h (Figure 15) show significant spatial variability that evidently has some relation with the presence of the separated jet. To examine that behavior further, we plot in Figure 16 horizontal fields on 1 August of relevant variables, including ageostrophic surface velocity vectors superposed on the relative vorticity ζ_g of the geostrophic surface currents, the maximum value in the upper 25 m of TKE, and the maximum value in the upper 25 m of the turbulent closure scheme stability function $G_h = min(-l^2N^2/2TKE, 0.028)$, where l is a turbulent length scale [e.g. *Wijesekera et al.*, 2003]. A relationship between the surface ageostrophic currents and the surface geostrophic vorticity is apparent in the horizontal fields. The direction of the surface ageostrophic velocity vectors is locally changed in areas of jet flows where the vorticity changes its sign (Figure 16, left). The across-jet sections (Figure 15c,g) indicate that the TKE is strongly affected by the ageostrophic processes in the surface layer. The horizontal field of the maximum value of TKE in the top 25 m (Figure 16, middle) gives an assessment of the spatial extent of that effect. Spatial variability in the near-surface TKE field has two distinguishable patterns. The relatively large values in the region south of Cape Blanco, with a maximum close to the shelf-break around 42 °N, have a spatial pattern closely related to that of the wind stress (Figure 13) and clearly represent the response of the surface layer TKE to the increased wind stress in that region. On the other hand, the zonally-oriented deep-red patch along 42 °N represents the TKE associated with the separated jet. The origin of the "jet-born" TKE pattern can be found in the area of negative vorticity north of the narrow strip of zero vorticity along the jet axis (Figure 16, left). The negative vorticity appears to affect the ageostrophic velocity, evidently contributing to an increase in its meridional component v_a close to the surface. This leads to increased vertical shear in v_a in the surface layer, visible in the offshore section along 126 °W (Figure 14i), and corresponding increased production of TKE (Figure 15g). The local increase in the TKE offshore just north of the jet axis consequently appears to be

forced in response to increased shear in the cross-jet ageostrophic velocity. Note that the dominant spatial variability in the near-surface TKE and hence in the depth of the surface boundary layer (SBL) is found on scales smaller than the scales of the wind stress. This finding suggests that the approach to obtain estimates of surface currents from the satellite information alone (SSH and wind stress), based on the assumption about the spatially uniform SBL depth [e.g., *Saraceno et al.*, 2008], can be limited in the CTZ.

To assess the spatial extent of unstable stratification indicated by the vertical sections of N^2 and K_h in Figure 15 we examine a horizontal field of the maximum of the stability function G_h [e.g. *Wijesekera et al.*, 2003], in the upper 25 m on 1 August-0800 (Figure 16, right). Negative values of G_h correspond to areas of stable stratification, while positive values correspond to areas of unstable stratification and result in accompanying large values of K_h. We note that there are extensive regions of positive G_h in the CTZ surface layer and that most of the patches of larger horizontal scale are offshore of 126 °W. In general, the patches of positive G_h (Figure 16, right) can be identified with areas where the surface flow direction is not aligned with the surface isopycnals (Figure 13, right) and the advection of heavier water over light water occurs. Note that these regions are not necessarily associated with the most energetic features of the surface velocities associated with the separated coastal jet.

4.5 Time-dependent behavior in the separated jet

In order to examine time-dependent behavior in the separated jet, we plot in Figure 17 horizontal fields of vertical velocities w at 25 m depth, the relative vorticity of the surface currents, and the surface potential density, with SSH contours superposed, on four days with variable wind conditions. The horizontal region of the plots encompasses the separated jet between (127 °W, 124.5 °W) and (41.7 °N, 42.7 °N). The days and the corresponding wind conditions (Figure 8) are as follows: 28 July-0000, moderately strong winds relatively early in a several-day southward wind event; 1 August-0800, strong winds

about 6 days into the same southward wind event; 6 August-0000, weak winds between southward wind events; 13 August-0000, strong winds about 6 days into a second strong southward wind event. Also plotted in Figure 17 is a measure of the flow imbalance

$$\epsilon = \frac{\partial(\nabla_h \cdot \mathbf{u})/\partial t}{f(|\zeta| + \overline{<\zeta^2>^{1/2}})}, \tag{5}$$

[*McWilliams*, 1985; compare *Capet et al.*, 2008b (16)], where $\nabla_h \cdot \mathbf{u} = u_x + v_y$ is the horizontal divergence of the surface velocity and $\zeta = v_x - u_y$ is the relative vorticity of the surface currents. The term $\overline{<\zeta^2>^{1/2}}$, where the brackets represent a spatial average over the horizontal sub-region shown and the overbar represents a time average over the period 26 July–21 August, is added to avoid singular behavior at zeros of ζ. Values of $|\epsilon| << 1$ indicate that the flow is essentially in balance, typically through a geostrophic or a more general gradient-wind balance. Values of $\epsilon = O(1)$ indicate that the flow is unbalanced.

We look first at the fields for 1 August-0800, which correspond to the same time as the sections in Figures 14 and 15 and the horizontal fields in Figures 13 and 16. The w field (Figure 17e) shows relatively small scale spatial variations along the jet with a wave length 20–30 km. These disturbances are found to propagate westward in the direction of the jet with a phase speed of about 25 km day^{-1} (Figure 18) and reflect the presence of submesoscale instabilities in the surface layer of the jet. From the sections in Figure 14, the magnitudes of the vertical velocities in these disturbances can reach values of 60 m day^{-1} at the near-coastal section and 40 m day^{-1} at the offshore section. The corresponding spatial variations in the surface vorticity field ζ (due mostly to the vorticity in the geostrophic surface currents), in the surface potential density field, and in the SSH field are relatively smooth, reflecting the larger scale jet structure, and do not give strong indications of variability on the smaller scales of the vertical velocity disturbances. The ϵ field has a spatial structure clearly related to that of the w field, with

magnitudes reaching around 0.5 in the regions of the large vertical velocities. Values of ϵ of that magnitude clearly indicate that these small-scale disturbances are not in either geostrophic or gradient-wind balance and that they are unbalanced. Note that evidence for the presence of the instabilities can be seen in the 1 August horizontal field of TKE (Figure 16) through the small scale fluctuations of TKE in the jet. In those fluctuations, the TKE values are generally reduced in the regions of upwelling velocities, as shown in the offshore section (Figures 14, 15).

During weak wind conditions on 6 August, the ζ field (Figure 17j) shows strong along-jet perturbations with a wave-like structure and an along-jet scale of about 50–70 km. These perturbations, also present in the surface potential density field, propagate along the jet with a phase speed of 25–30 km day^{-1}. In contrast to the behavior on 1 August, the w field (Figure 17i) along the jet exhibits weaker variability, and smaller magnitudes. The largest magnitudes of w are associated with downwelling and are found near the crests of the along-front instabilities (Figure 17k), where the curvature of the SSH field is locally large. The ϵ values are relatively low (Figure 17l) with two spots of increased values, also near the crests. The instabilities present on this day appear to have a different dynamical structure than those found during strong winds on 1 August and, from the ϵ fields, to be essentially balanced.

During the second strong wind event on 13 August the small-scale, unbalanced instabilities are again present with substantial fluctuations in the w field, accompanied by related variations in ϵ (Figure 17p), propagating along the jet (Figure 18), similar to those on 1 August. Fluctuations in the surface vorticity field and in the surface potential density field, however, are larger than those on 1 August, with some resemblance to those present during weak winds on 6 August. Two days after this event on 15 August, the small-scale, unbalanced instabilities decay (not shown here) and the vorticity and density fields become very much like those on 6 August, with similar disturbances of wave-like structure. Thus, there are some indications that the small-scale, unbalanced instabilities

may subsequently evolve into the larger scale, balanced instabilities.

In order to examine the generation and propagation of the small-scale, unbalanced instabilities shown in Figure 17e,m, we construct a *Hovmöller* diagram of the time dependent vertical velocities w at 25 m depth, sampled along the mean path of maximum density gradient $|\nabla_h \rho|$ representing the jet axis, for two time intervals when those instabilities are present: 28 July–9 August and 10–22 August (Figure 18). During the first time interval, strong instabilities, identified by large magnitude vertical velocities (up to 60 m day^{-1}), start to develop on 30 July. They propagate along the jet path and stay in the subdomain until 4 August. Most of instabilities during that interval originate between 50 and 100 km from the start point of the jet path in a region where the jet is still mainly flowing toward the south before turning offshore (see the plot of the mean path in Figure 18). If we consider individual perturbations, then the lifetime of a perturbation, defined as the time when the magnitude of w is greater than 25 m day^{-1}, can be estimated to be around 3 days and the distance traveled to be around 75 km, which gives an average propagation speed of 25 km day^{-1}. During the second time period of instability occurrence, more instabilities originate closer to the start point of the jet path, and not all of them travel all the way to the offshore part of the subdomain. Instabilities are present in the subdomain from 11 to 17 August. They are characterized by larger vertical velocities up to 100 m day^{-1}, longer lifetimes around 4 days, and by smaller average propagation speeds of 18 km day^{-1}.

To further examine the time-dependent relationship of the relatively large fluctuations in vertical velocity, that contribute to the horizontal fields of mean and standard deviation of w in Figure 10, with the occurrence of the submesoscale instabilities, we calculate the spatial average (again denoted by brackets) of the vertical velocity squared $< w^2 >$ at 25 m depth and surface vorticity squared $< \zeta^2 >$ over the sub-region around the offshore separated jet shown in Figure 17. Those values, together with the magnitude of wind stress, are plotted as time series for 26 July–22 August in Figure 19. Two

events of large $< w^2 >$ occur, on 3 and 13 August, respectively. These events coincide with the presence of the small-scale, unbalanced instabilities. The lagged relation of the larger values of $< w^2 >$, with larger values of the southward wind stress is clear. (The maximum correlation coefficient of $< w^2 >$ and $|\tau^y|$ is 0.62 at a lag of 2 days.) The two events of large $< w^2 >$ are followed by increased $< \zeta^2 >$ with about 2 days lag. This evidently reflects the weakening of the small-scale, unbalanced instabilities and the subsequent growth of, or evolution into, the larger scale balanced instabilities, characterized by substantial fluctuations in vorticity.

4.6 Frontogenesis along the separated jet

In order to assess the frontogenesis along the separated jet we use frontogenesis function F following *Capet et al.*, 2008b:

$$\frac{D|\nabla_h \rho|^2}{Dt} = 2F, \tag{6}$$

where $|\nabla_h \rho|^2 = (\partial\rho/\partial x)^2 + (\partial\rho/\partial y)^2$ is the absolute value of surface density gradient squared. Horizontal fields of the kinetic energy of surface currents $KE = 0.5(u^2 + v^2)$, $|\nabla_h \rho|^2$, and the part of F due to horizontal advection [*Hoskins*, 1982; *Capet et al.*, 2008b]:

$$F_s = -\left(\frac{\partial u}{\partial x}\left(\frac{\partial \rho}{\partial x}\right)^2 + \frac{\partial v}{\partial y}\left(\frac{\partial \rho}{\partial y}\right)^2 + \left(\frac{\partial v}{\partial x} + \frac{\partial u}{\partial y}\right)\frac{\partial \rho}{\partial x}\frac{\partial \rho}{\partial y} \right), \tag{7}$$

averaged in time over the 27 day period 26 July–21 August are shown in Figure 20. The structure of the surface kinetic energy field is remarkable in that by far the largest values over the entire domain are concentrated in the region of the separated jet offshore south of Cape Blanco. Dynamically consistent large values of the absolute value of the horizontal gradient of the surface density squared $|\nabla_h \rho|^2$ are also found concentrated along the jet in the same region. The largest values of $|\nabla_h \rho|^2$ occur, however, near the coast between

42.5 °N and 43 °N, where the jet is still flowing south in the general direction of the wind stress. The large values of $|\nabla_h \rho|^2$ in the separated jet are clearly related to the concentrated large mean values of the frontogenesis function F_s found in the same region. In particular, there is an obvious match between the increased magnitudes of both fields in the jet near the coast between 42.5 °N and 43 °N. It appears that frontogenesis processes related to the CTZ flow fields play a major role in establishing the structure and intensity of the separated jet. In the near-shore southward flowing part of the jet, frontogenesis processes, intensified by the along-jet wind stress, contribute directly to the development of the FSC. In the offshore part of the jet, frontogenesis processes influence the structure of the jet and thus affect the behavior of the submesoscale instabilities. Consequently, in both parts of the jet, frontogenesis processes play a role in the maintenance of the concentrated large mean and RMS vertical velocities shown in Figure 10.

To document one additional aspect of the behavior of the vertical velocities, regarding possible differences in the maximum magnitudes of the downwelling and upwelling velocities, we calculate probability density functions (PDFs) of the extreme positive and negative values of w over the top 80 m depth and over the time period 26 July–21 August (Figure 21). Two horizontal regions are selected, one for the near-coastal part of the jet, where it is flowing southward in the direction of the wind stress, and one for the offshore part, where it flows westward. The near-coastal region extends from 42.3 °N – 43 °N and includes all values along east-west grid lines 18 km on either side of the jet axis, defined by the mean location of the maximum surface velocity. The offshore section extends from 125.7 °W – 126.3 °N and includes all values along north-south grid lines 18 km on either side of the jet axis. From Figure 21a we can see that in the near-coastal region, where the down-front winds evidently contribute to an increase in the absolute values of surface density gradients (Figure 20) and to an intensification of the accompanying FSC (Figure 10), the positive upwelling velocities clearly have more occurrences of larger magnitude than do the negative downwelling velocities. Thus, in this region we find typically

stronger upwelling velocities and weaker downwelling velocities. Consistent with that result, stronger upwelling velocities are evident in the instantaneous near-coastal section in Figure 14. The behavior differs, however, in the offshore region (Figure 21b), where the downwelling velocities have more occurrences of larger magnitude than the upwelling velocities. Thus, in the offshore region, where the wind stress is normal to the direction of the jet and where the more energetic vertical circulation appears to be primarily associated with time-dependent, submesoscale instabilities, we find evidence for typically stronger downwelling velocities. That general behavior is also consistent with the model results of *Capet, et al.* [2008b] and with theoretical results [*Hoskins*, 1982] concerning the FSC associated with frontogenesis caused by larger scale horizontal deformation fields.

5 Discussion

The phenomenon of nonlinear interaction between effects of a geostrophic flow and a wind stress applied to a surface Ekman layer has been studied in a number of papers [*Stern*, 1965; *Niiler*, 1969; *Thomas and Rhines*, 2002; *Thomas and Lee*, 2005; *Pedlosky*, 2008]. *Lee et al.* [1994] used a two-dimensional numerical model to study the case when a spatially uniform wind is applied both along and across a geostrophically balanced jet. They reported secondary circulation that is created as a result of a nonlinear interaction between the jet and the wind driven flow in the Ekman layer. In that study (as well as studies mentioned above) an expression similar to equation (4) for the Ekman transport M_E was used. They found that when the wind blows perpendicular to the jet the secondary circulation is 50 % weaker than that when the wind blows parallel to the jet, with upward vertical advection on the upwind side of the jet ($\zeta < 0$) and downward advection on downwind side ($\zeta > 0$). *Lee and Niiler* [1998] modeled the ocean response to uniform wind stress forcing over geostrophically balanced eddies. Their results for the mean secondary circulation, were consistent with the features found in *Lee et al.* [1994]. *Centurioni et al.* [2008] used surface drifter data, satellite SSH measurements, and NCEP reanalysis

winds to map the time-average 15 m depth geostrophic velocity field in the CCS. The resultant mean circulation and eddy energy distributions were found to be in reasonable agreement with ROMS CCS model results from *Marchesiello et al.* [2003]. Analysis of the time-average near-surface ageostrophic velocity field in the ROMS CCS solutions showed behavior similar to that found in *Lee and Niiler* [1998] and thus was argued to be associated with the nonlinear interaction of Ekman dynamics with the geostrophic vorticity field. *Pedlosky* [2008], in an analytical study for a homogeneous fluid, determined the nonlinear effects of geostrophic vorticity ζ_g and wind stress curl on the Ekman layer thickness. The importance of accounting for the Ekman layer depth for calculations of surface velocity from satellite SSH measurements was noted in Section 4.4. *Thomas and Lee* [2005] studied the effect of strong winds blowing in the direction of a frontal jet on frontogenesis and found that the frontogenesis secondary circulation, characterized by subduction on the dense side of the front and upwelling along the frontal interface, is intensified. The results of that study appear especially relevant to the behavior found here in the near-coastal region of the separated jet where it flows southward in the direction of the wind stress. Our simulations of the 3D dynamics of the jet in Oregon CTZ, however, contain a more complicated set of time- and space-dependent dynamical processes than those represented in most of these idealized model investigations. Additional process-oriented studies in a realistic CTZ environment would be useful.

The behavior and the dynamics of circulation processes near the ocean surface have been addressed further in several recent studies [*Capet et al.*, 2008a,b,c; *Lapeyre and Klein*, 2006; *Lapeyre et al.*, 2006; *Klein et al.*, 2008; *Boccaletti et al.*, 2007; *Fox-Kemper et al.*, 2008; *Fox-Kemper and Ferrari*, 2008]. In particular, the subject of near-surface vertical exchange associated with submesoscale processes has been discussed in a useful recent review paper by *Klein and Lapeyre* [2009]. The previous results of most relevance here are those of *Capet et al.* [2008a,b,c] where the dynamics of near surface submesoscale processes in an idealized eastern boundary current oceanic regime with steady wind forcing

was investigated. In particular, *Capet et al.* [2008b] found evidence for more intense FSC in fronts oriented in the downwind direction, consistent with the results of *Thomas and Lee* [2005] and in agreement with the behavior found here in the near-coastal southward flowing part of the separated coastal jet. *Capet et al.* [2008b] also found evidence for frontogenesis processes associated with regions of large surface density gradients, similar to the behavior shown here in Figure 20. In addition, *Capet et al.* [2008b] found occurrences of submesoscale instability growth and propagation along fronts with instability wavelengths of 20–30 km. The instabilities were characterized by spatial variations in the surface potential density σ_θ and by increases in magnitude of corresponding submesoscale surface vorticity ζ fluctuations. The small-scale, unbalanced instabilities found here (Figures 17,18) have similar spatial scales, but appear to be characterized most strongly by substantial fluctuations in w, resulting in vigorous vertical exchange in the surface layer (Figure 14j), with relatively smaller variations in ζ. Moreover, there is a clear relation between increased strength of the wind stress and occurrence of these instabilities (Figure 19). To what extent the development of these instabilities depend on the wind stress through resultant changes in the structure of the separated jet, or on the increase in magnitude of the surface layer ageostrophic transport, or on their interaction, is not clear from these simulations. Additional controlled process studies to address these questions would be useful. In contrast, the somewhat larger scale instabilities found on 6 August are characterized by substantial variations in surface ζ and σ_θ and by a larger degree of balance (Figure 17j,k,l).

We note that the primary differences in the results of our limited-time simulation of late summer conditions, with realistic wind stress forcing and realistic coastal topography, and those from the longer-time simulations of *Capet et al.* [2008a,b,c], with more idealized forcing and topography, is in the strong space- and time-dependent behavior found here. In particular, the significant spatial concentration of the near-surface ageostrophic vertical circulation processes in the region of the separated coastal jet off Cape Blanco (Figure 10)

and the time dependent behavior of that circulation in response to the wind stress forcing (Figure 19), appears to identify potentially important components of realistic CTZ flow fields off Oregon and northern California.

6 Summary

Based on comparisons with different types of data, our 3D nonlinear model describes the dynamics both on the shelf and in the CTZ off Oregon qualitatively correctly. Comparisons with currents at mid-shelf moorings indicate that the model reproduces both depth-averaged and baroclinic dynamics on the shelf. The modeled SST front evolution is consistent with satellite SST fields showing the major feature of summer-time Oregon CTZ dynamics, such as the separation of the coastal jet near Cape Blanco. HF radar measurements of surface currents (Figure 6) provide evidence that the observed jet that separates off Cape Blanco is as energetic as the modeled separating jet with maximum speeds reaching 0.6–0.8 m s^{-1}. Lagrangian analysis reveals characteristic flow patterns over the shelf and in the CTZ off Oregon, in particular, separated jets near Heceta Bank and Cape Blanco.

The behavior of near-surface circulation in the CTZ off Oregon during a late-summer 27 day time period, 26 July–21 August, was investigated. Significant vertical velocities were found concentrated in the region of the separated jet south of Cape Blanco. In the near-coastal part of the separated jet, where it was flowing southward in the direction of the winds, the wind stress appeared to intensify the frontogenesis secondary circulation. The associated instantaneous vertical velocities were as large as 100 m day^{-1}. In the offshore part of the separated jet, where it was flowing westward, the energetic vertical velocities were primarily associated with time-dependent submesoscale instabilities. Those instabilities were present during strong southward wind events. They propagated in the direction of the jet with wavelengths 20–30 km and propagation speeds of 18–25 km day^{-1}. The larger vertical velocities were typically 50 m day^{-1}.

As a next step, it would be useful to extend these analyses to a coupled bio-physical model, to see how the surface layer processes within the jet affect biological variability.

Acknowledgments. This is Contribution Number 658 of the U.S. GLOBEC program, jointly funded by the National Science Foundation and the National Oceanic and Atmospheric Administration. We gratefully acknowledge support for this research by the U.S. GLOBEC-NEP Project and by the Cooperative Institute for Oceanographic Satellite Studies, which is supported by the National Oceanic and Atmospheric Administration, both through award NA03NES4400001, and the Office of Naval Research Physical Oceanography project, award number N000140810942. The GLOBEC-NEP mooring data at Coos Bay and Rogue River were provided by B. M. Hickey and S. R. Ramp. Data for NH10 GLOBEC mooring and HF-radar measurements were provided by P. M. Kosro. Satellite information on SST was provided by P. T. Strub. Data on SeaSoar density measurements were provided by J. A. Barth. The NCOM model results were supplied by I. Shulman. We thank all the above investigators. We also thank S. R. Springer for the help in model set up and G. D. Egbert and R. N. Miller for thoughtful discussions. We are especially grateful to two anonymous reviewers for constructive and helpful comments that led to substantial positive revisions in an initial manuscript.

References

Allen, J., P. Newberger, and J. Federiuk (1995), Upwelling Circulation on the Oregon Continental Shelf. Part I: Response to Idealized Forcing. *J. Phys. Oceanogr.*, *25*, 1843–1866.

Barth, J. A., S. D. Pierce, and T. J. Cowles (2005), Mesoscale structure and its seasonal evolution in the Northern California Current System, it Deep-Sea Res. II,*52*, 5–28.

Barth, J. A., S. D. Pierce, and R. L. Smith (2000), A separating coastal upwelling jet

at Cape Blanco, Oregon and its connection to the California Current System. it Deep-Sea Res. II, *47*, 783–810.

Barth, J. A., and P. A. Wheeler (2005), Introduction to special section: Coastal Advances in Shelf Transport. *J. Geophys. Res.*, *110*, C10S01, doi:10.1029/2005JC003124.

Batchelor, G.K. (1967), *An Introduction to Fluid Dynamics.*, 615 pp., Cambridge Univ. Press, New York.

Boccaletti, G., R. Ferrari, and B. Fox-Kemper (2007), Mixed Layer Instabilities and restratification. *J. Phys. Oceanogr.*, *37*, 2228–2250.

Brink, K. H., T. J. Cowles (1991), The Coastal Transition Zone program. *J. Phys. Oceanogr.*, *96*, 14637–14647.

Capet, X., J.C. McWilliams, M.J. Molemaker, and A.F. Shchepetkin (2008a), Mesoscale to Submesoscale Transition in the California Current System. Part I: Flow Structure, Eddy Flux, and Observational Tests. *J. Phys. Oceanogr.*, *38*, 29–43.

Capet, X., J.C. McWilliams, M.J. Molemaker, and A.F. Shchepetkin (2008b), Mesoscale to Submesoscale Transition in the California Current System. Part II: Frontal Processes. *J. Phys. Oceanogr.*, *38*, 44–64.

Capet, X., J.C. McWilliams, M.J. Molemaker, and A.F. Shchepetkin (2008c), Mesoscale to Submesoscale Transition in the California Current System. Part III: Energy Balance and Flux. *J. Phys. Oceanogr.*, *38*, 2256–2269.

Castelao, R.M., and J.A. Barth (2007), The Role of Wind Stress Curl in Jet Separation at a Cape. *J. Phys. Oceanogr.*, *37*, 2652–2671.

Centurioni, L.R., J.C. Ohlmann, P.P. Niiler (2008), Permanent Meanders in the California Current System. *J. Phys. Oceanogr.*, *38*, 1690–1710.

Chapman, D. C. (1985), Numerical treatment of cross-shelf open boundaries in a barotropic coastal ocean model. *J. Phys. Oceanogr.*, *15*, 1060–1075.

Dewey, R. K., J. N. Moum, C. A. Paulson, D. R. Caldwell, and S. D. Pierce (1991), Structure and dynamics of a coastal filament. *J. Geophys. Res.*, *96*(C8), 14885–14907.

Di Lorenzo, E. (2003), Seasonal dynamics of the surface circulation in the Southern California Current System. *Deep-Sea Res. II*: Topical Studies in Oceanography, *50*, 2371–2388.

Fairall, C.W., E.F. Bradley, J.E. Hare, A.A. Grachev, and J.B. Edson (2003), Bulk Parameterization of Air-Sea Fluxes: Updates and Verification for the COARE Algorithm. *J. Climate*, *16*, 571–591.

Flather, R.A. (1976), A tidal model of the north-west European continental shelf. *Mem. Soc. R. Sci. Liège.*, *6*, 141–164.

Fox-Kemper, B., R. Ferrari, and R.W. Hallberg (2008a), Parameterization of Mixed Layer Eddies. Part I: Theory and Diagnosis. *J. Phys. Oceanogr.*, *38*, 1145–1165.

Fox-Kemper, B., and R. Ferrari (2008b), Parameterization of Mixed Layer Eddies. Part I: Prognosis and Impact. *J. Phys. Oceanogr.*, *38*, 1166–1179.

Fu, L.-L., E. J. Christensen, C. A. Yamarone, M. Lefebvre, Y. Menard, M. Dorrer, and P. Escudier (1994), TOPEX/POSEIDON Mission Overview. *J. Geophys. Res.*, *99*, 24369–24381.

Galperin, B., L. H. Kantha, S. Hassid, and A. Rosati (1988), A quasi-equilibrium turbulent energy model for geophysical flows. *J. Atm. Sci.*, *45*, 55–62.

Gan, J., and J. S. Allen (2002), A modeling study of shelf circulation off northern California in the region of the Coastal Ocean Dynamics Experiment, 2, Simu-

lations and comparisons with observations. *J. Geophys. Res.*, *107*(C11), 3184, doi:10.1029/2001JC001190.

Haidvogel, D. B., J. Blanton, J. C. Kindle, D. R. Lynch (2000), Coastal ocean modeling: processes and real-time systems. *Oceanography*, *13*, 35–46.

Hickey, B. M., S. Geier, N. Kachel, S. Ramp, and P. M. Kosro (2009), Seasonal Water Properties and Velocity in the Northern California Current: Interannual Variability and Alongcoast Structure. Submitted to *Limnology and Oceanography.*

Hodur, R.M. (1997), The Naval Research Laboratory's Coupled Ocean/Atmosphere Mesoscale Prediction System (COAMPS). *Mon. Wea. Rev.*, *125*, 1414–1430.

Hoskins, B.J. (1982), The mathematical theory of frontogenesis. *Annu. Rev. Fluid Mech.*, *14*, 131–151.

Kalnay, E., M. Kanamitsu, R. Kistler, W. Collins, D. Deaven, L. Gandin, M. Iredell, S. Saha, G. White, J. Woollen, Y. Zhu, A. Leetmaa, R. Reynolds, M. Chelliah, W. Ebisuzaki, W. Higgins, J. Janowiak, K. Mo, C. Ropelewski, J. Wang, R. Jenne, and D. Joseph (1996), The NCEP/NCAR 40-Year Reanalysis Project. *Bull. Amer. Meteor. Soc.*, *77*, 437–471.

Kadko, D. C., L. Washburn, and B. Jones (1991), Evidence of subduction within cold filaments of the Northern California Coastal transition Zone. *J. Phys. Oceanogr.*, *96*, 14909–14926.

Klein, P., B. Hua, G. Lapeyre, X. Capet, S. Le Gentil, and H. Sasaki (2008), Upper Ocean Turbulence from High-Resolution 3D Simulations. *J. Phys. Oceanogr.*, *38*, 1748–1763.

Klein, P. and G. Lapeyre, (2009), The oceanic vertical pump induced by mesoscale and submesoscale turbulence. *Ann. Rev. Mar. Sci.*, *1*, 351–375.

Kosro, P. M. (2003), Enhanced southward flow over the Oregon shelf in 2002: A conduit for subarctic water, *Geophys. Res. Lett.*, *30*(15), 8023, doi:10.1029/2003GL017436.

Kosro, P. M. (2005), On the spatial structure of coastal circulation off Newport, Oregon, during spring and summer 2001 in a region of varying shelf width. *J. Geophys. Res.*, *110*, C10S06, doi:10.1029/2004JC002769.

Lapeyre, G. and P. Klein (2006), Dynamics of the upper oceanic layers in terms of surface quasigeostrophy theory. *J. Phys. Oceanogr.*, *36*, 165–176.

Lapeyre, G., P. Klein, and B. Hua (2006), Oceanic restratification forced by surface frontogenesis. *J. Phys. Oceanogr.*, *36*, 1577–1590.

Lee, D., P. Niiler, A. Warn-Varnas, and S. Piacsek (1994), Wind-driven secondary circulation in ocean mesoscale. *J. Mar. Res.*, *52*, 371–396.

Lee, D.-K., and P. P. Niiler (1998), The inertial chimney: The near-inertial energy drainage from the ocean surface to the deep layer. *J. Geophys. Res.*, *103*(C4), 7579–7591.

Marchesiello, P., J.C. McWilliams, and A. Shchepetkin (2001), Open boundary conditions for long-term integration of regional oceanic models. *Ocean Modelling*, *3*, 1–20.

Marchesiello, P., J.C. McWilliams, and A. Shchepetkin (2003), Equilibrium Structure and Dynamics of the California Current System. *J. Phys. Oceanogr.*, *33*, 753–783.

Maturi, E., A. Harris, C. Merchant, J. Mittaz, B. Potash, W. Meng, and J. Sapper (2008), NOAA's Sea Surface Temperature Products From Operational Geostationary Satellites. *Bull. Amer. Meteor. Soc.*, *89*, 1877–1888.

McWilliams J. C. (1985), A uniformly valid model spanning the regimes of geostrophic

and isotropic, stratified turbulence: Balanced turbulence. *J. Atm. Sci.*, *42*, 1773–1774.

Mellor, G. L., and T. Yamada (1982), Development of a turbulence closure model for geophysical fluid problems. *Rev. Geophys. Space Phys.*, *20*, 851–875.

Niiler, P. P. (1969), On the Ekman divergence in an oceanic jet. *J. Geophys. Res.*, *74*, 7048–7052.

National Geophysical Data Center (1988), Digital relief of the surface of the Earth, *Data Announce. 88-MGG-02*, NOAA, Boulder, Colo.

O'Malley, R., Barth, J.A., Cowles, T.J., Pierce, S.D., Wingard, C (2002) SeaSoar CTD observations during the GLOBEC Northeast Pacific mesoscale surveys I, II, III and IV. WWW Page, http://damp.coas.oregonstate.edu/globec/nep/seasoar.

Paduan, J. D., P. M. Kosro, S. M. Glenn (2004), A National coastal ocean surface current mapping system for the United States. *Mar. Tech. Soc. J.*, *38*, 102–108.

Pedlosky, J. (1987), *Geophysical Fluid Dynamics.*, 710 pp., Springer Verlag, New York.

Pedlosky, J. (2008), On the weakly nonlinear Ekman layer: thickness and flux. *J. Phys. Oceanogr.*, *38*, 1334–1339.

Ramp, S. R., and F. L. Bahr (2008), Seasonal Evolution of the Upwelling Process South of Cape Blanco. *J. Phys. Oceanogr.*, *38*, 3–28.

Samelson, R., P. Barbour, J. Barth, S. Bielli, T. Boyd, D. Chelton, P. Kosro, M. Levine, E. Skyllingstad, and J. Wilczak (2002), Wind stress forcing of the Oregon coastal ocean during the 1999 upwelling season. *J. Geophys. Res.*, *107*(C5), doi:10.1029/2001JC000900.

Saraceno, M., P. T. Strub, and P. M. Kosro (2008), Estimates of sea surface height and near-surface alongshore coastal currents from combinations of altimeters and tide gauges *J. Geophys. Res.*, *113*, C11013, doi:10.1029/2008JC004756.

Shchepetkin, A. F., and J. C. McWilliams (2003), A method for computing horizontal pressure-gradient force in an oceanic model with a nonaligned vertical coordinate. *J. Geophys. Res.*, *108*(C3), 3090, doi:10.1029/2001JC001047.

Shchepetkin, A. F., and J. C.McWilliams (2005), The Regional Ocean Modeling System: A split-explicit, free-surface, topography-following-coordinate oceanic model. *Ocean Modelling*, *9*, 347–404, doi:10.106/j.oceanmod.2004.08.002.

Shulman, I., J. C. Kindle, S. deRada, S. C. Anderson, B. Penta, and P. J. Martin (2004), Development of a Hierarchy of Nested Models to Study the California Current System. In: Malcolm L., and P. E. Spaulding (Eds.), 2003: Estuarine and Coastal Modeling. Proc. of the 8^{th} International Conference on Estuarine and Coastal Modeling, November 3–5, 2003, Monterey, CA., 74–88, doi 10.1061/40734(145)6.

Shulman, I., J. Kindle, P. Martin, S. deRada, J. Doyle, B. Penta, S. Anderson, F. Chavez, J. Paduan, and S. Ramp (2007), Modeling of upwelling/relaxation events with the Navy Coastal Ocean Model. *J. Geophys. Res.*, *112*, C06023, doi:10.1029/2006JC003946.

Springer, S. R., R. M. Samelson, J. S. Allen, G. D. Egbert, A. L. Kurapov, R. N. Miller, and J. C. Kindle (2009), A nested grid model of the Oregon coastal transition zone: Simulations and comparisons with observations during the 2001 upwelling season. *J. Geophys. Res.*, *114*, C02010, doi:2008JC004863.

Stern, M. E. (1965), Interaction of a uniform wind stress with a geostrophic vortex. *Deep Sea Res.*, *12*, 355–367.

Strub, P. T., H. P. Batchelder, and T. J. Weingartner (2002), U.S. GLOBEC Northeast Pacific Program: Overview. *Oceanography*, *15*, 30–35.

Strub, P. T., P. M. Kosro, and A. Huyer (1991), The nature of the cold filaments in the California Current System. *J. Phys. Oceanogr.*, *96*, 14743–14768.

Thomas, L. N., and P. B. Rhines (2002), Nonlinear stratified spin-up. *J. Fluid Mech.*, *473*, 211–244.

Thomas, L. N., and C. M. Lee (2005), Intensification of ocean fronts by down-front winds. *J. Phys. Oceanogr.*, *35*, 1086–1102.

Washburn, L., D. C. Kadko, B. H. Jones, T. Hayward, P. M. Kosro, T. P. Stanton, S. Ramp, and T. Cowles (1991), Water mass subduction and the transport of phytoplankton in a coastal upwelling system *J. Phys. Oceanogr.*, *96*, 14927–14946.

Wijesekera, H. W., J. S. Allen, and P. A. Newberger, 2003: Modeling study of turbulent mixing over the continental shelf: Comparison of turbulent closure schemes. *J. Geophys. Res.*, **108**, 3103, doi:10.1029/2001JC001234.

Figure 1: Monthly SST composites from GOES satellite (top) and monthly averaged SST from ROMS (bottom) for May–August (left to right). Coastal HF radar locations are shown in the lower right panel by blue circles, and mid-shelf moorings by magenta circles. 'CB' denotes Cape Blanco. The black line shows the 200 m isobath.

Figure 2: Along-shore COAMPS wind stress τ^y at the NH10 (44.6 °N) (a) and Rogue River (42.4 °N) (b) moorings; and depth-averaged along-shore current V at NH10 (44.6 °N) (c), Coos Bay (43.2 °N) (d), and Rogue River (42.4 °N) (e) mooring observations (gray lines) and model (black lines). Variables are presented along respective major principal axes. Root mean square error (RMSE) and correlation coefficients (CC) for data and model are shown.

Figure 3: Mean and variance ellipses for depth-averaged currents at the mooring locations (top to bottom: NH10, Coos Bay, Rogue River) for observations (gray), and model (black) over the calculation interval (see Figure 2).

Figure 4: Vertical profiles of time-averaged statistics for cross-shore u (pale colors, thick lines) and along-shore v (bright colors, thin lines) components of velocity projected on respective principal axes of the depth-averaged velocities: means (a), standard deviations (std) (b), normalized root mean square error (NRMSE) (c), defined as $NRMSE = \left[\overline{(u_{obs} - u_{mod})^2}/\overline{u_{obs}^2}\right]^{\frac{1}{2}}$, where the over-bar denotes a time-average, correlation coefficients (CC) (d). In (a) and (b), red lines denote observations, blue lines – model results. Data is taken from mid-shelf moorings: NH10 (top), Coos Bay (middle), and Rogue River (bottom).

Figure 5: Surface current statistics from HF radar and model for May–August (top to bottom): two left panels – monthly averaged current vectors $\mathbf{u}$ and speed $|\mathbf{u}|$ in color; two right panels – RMS speed deviations from the mean $U_{RMS} = \left[\overline{(u-\bar{u})^2 + (v-\bar{v})^2}\right]^{\frac{1}{2}}$, where the over-bar denotes a time-average. Color contour intervals for U_{RMS} are 0.03 m s^{-1}. The white contour on the model fields shows the area of the corresponding data coverage.

Figure 6: Instantaneous fields of surface current vectors $\mathbf{u}$ and speed $|\mathbf{u}|$ (color) for HF radar (top panel) and model (middle panel) in July–August in the area near Cape Blanco, and observed satellite SSH (from track 206) (red) and model SSH sampled at the same location (blue) shown in the bottom panels. The SSH has the mean taken out. The location of track 206 is denoted by a white dashed line.

Figure 7: Cross-shore sections of potential density σ_θ measured during a SeaSoar survey (a,c,e), and model fields (b,d,f) sampled at the same times and locations as the observations, along 44.25 °N during 2 August (a,b), 43.5 °N during 3–4 August (c,d) and 41.9 °N during 6–7 August (e,f). Color contour intervals are 0.25 kg m^{-3}.

Figure 8: Time series of the north-south component of the wind stress τ^y, averaged over the across-jet section along 126 °W between 41.65 °N and 42.4 °N (see Figure 13), from 26 July–31 August 2002. Black-shaded bars denote strong wind events, gray-shaded bars – weak wind events.

Figure 9: Surface potential density σ_θ in color and SSH in white contours (left) and surface current vectors $\mathbf{u}$ and their standard deviations in color (right), averaged over 26 July–21 August. Contour intervals for SSH are 0.03 m. The solid black line shows the 200 m isobath.

Figure 10: Mean vertical velocity w at 25 m depth (left) and its standard deviation (right) in color and SSH in black contours, averaged over 26 July–21 August. Contour intervals for SSH are 0.03 m. The solid black line shows the 200 m isobath.

Figure 11: Lagrangian surface particle trajectories (gray lines) during 1–10 August (left) and 1–20 August (right). Particles are released simultaneously on 1 August along the 81 m isobath (depth of NH10 mooring) every 10 km in the meridional direction. Circles denote particles final locations if they are within the domain. The coastline is shown in bold, isobaths 100, 200, and 1000 m – in thin black lines.

Figure 12: Divergence (a,c) and deformation (b,d) terms of the surface strain rate field (3) averaged over 26 July–21 August (a,b) and on 1 August-0800 (c,d). The solid black line shows the 200 m isobath.

Figure 13: Surface wind stress magnitudes in color and directions in vectors (left), surface potential density in color and surface velocity $\mathbf{u}$ in vectors (right) on 1 August-0800. Cross-jet section locations along 42.63 °N and 126 °W, respectively, are shown (right) by straight lines where the middle tick denotes the jet axis location. The solid black line shows the 200 m isobath.

Figure 14: Cross-jet near-coastal (a–e) and offshore (f–j) sections on 1 August-0800: potential density (a,f), geostrophic v_g (b), u_g (g) and ageostrophic v_a (c), u_a (h) components of along-jet velocity, ageostrophic component of the cross-jet velocity u_a (d), v_a (i) and vertical velocity w (e,j). Color contour intervals are 0.1 kg m^{-3} for σ_θ, 0.05 m s^{-1} for (u_g, v_g), 0.025 m s^{-1} for (u_a, v_a) and 5 m day^{-1} for w. Bold isolines denote zero velocity. The near-coastal cross-jet section is along 42.63 °N, and the offshore section is along 126 °W (see Figure 13).

Figure 15: Cross-jet near-coastal (a–d) and offshore (e–h) sections on 1 August-0800: buoyancy frequency N^2 (a,e), vertical turbulent diffusivity coefficient K_h (b,f), turbulent kinetic energy in color, Richardson number $Ri = N^2/S^2$ in white contours (c,g) and shear production $P = K_m S^2$ (d,h). Negative values of N^2 are shown with white stars. The near-coastal cross-jet section is along 42.63 °N, and the offshore section is along 126 °W (see Figure 13).

Figure 16: Ageostrophic component of the surface current $\mathbf{u_a}$ in vectors and relative vorticity of geostrophic surface current ζ_g in color (left), maximum of turbulent kinetic energy in upper 25 m in color and SSH in contours (middle), maximum of the stability function G_h in upper 25 m (right) on 1 August-0800. The solid black and white lines show the 200 m isobath.

Figure 17: Vertical velocity at 25 m depth w (a,e,i,m), relative vorticity of the surface current ζ (b,f,j,n), surface potential density σ_θ (c,g,k,o) and a measure of the imbalance ϵ (d,h,l,p) (see (5) Section 4.5) for the area around the separated jet on 28 July-0000 (a–d), 1 August-0800 (e–h), 6 August-0000 (i–l), 13 August-0000 (m–p). Black and white contours show the SSH with contour intervals 0.02 m.

Figure 18: *Hovmöller* diagrams of w at 25 m sampled along the jet path (shown in small windows), as determined from the mean location of the maximum in $|\nabla_h \rho|$, for two time intervals of instability occurrence.

Figure 19: Time series plots of the spatial average, denoted by brackets, over the region around the separated jet shown in Figure 17 of $< w^2 >$ at 25 m (m^2 s^{-2}x10^{-8}) (red line) and surface $< \zeta^2 >$ (s^{-2}x5x10^{-10}) (blue line). Also, plotted is the corresponding time series of $|\tau^y|$ (N m^{-2}) (gray line) calculated as in Figure 8.

Figure 20: Kinetic energy of surface current (left), absolute value of the horizontal gradient of surface density squared $|\nabla_h \rho|^2$ (middle) and the frontogenesis function F_s (7) (right), averaged over 26 July–21 August. The solid black line shows the 200 m isobath.

Figure 21: Histogram of the extreme positive and negative values of the vertical velocity w over the top 80 m depth across the coastal jet in its near-coastal (a) and offshore (b) parts. The near-coastal part of the jet for this sampling extends from $42.2\,^{\circ}\mathrm{N} - 43\,^{\circ}\mathrm{N}$ and the offshore part extends from $125.7\,^{\circ}\mathrm{W} - 126.3\,^{\circ}\mathrm{W}$. The sampling is made in a 36-km band, centered along the jet axis, defined here by the mean location of the maximum surface velocity, and the integration interval is from 26 July–21 August.

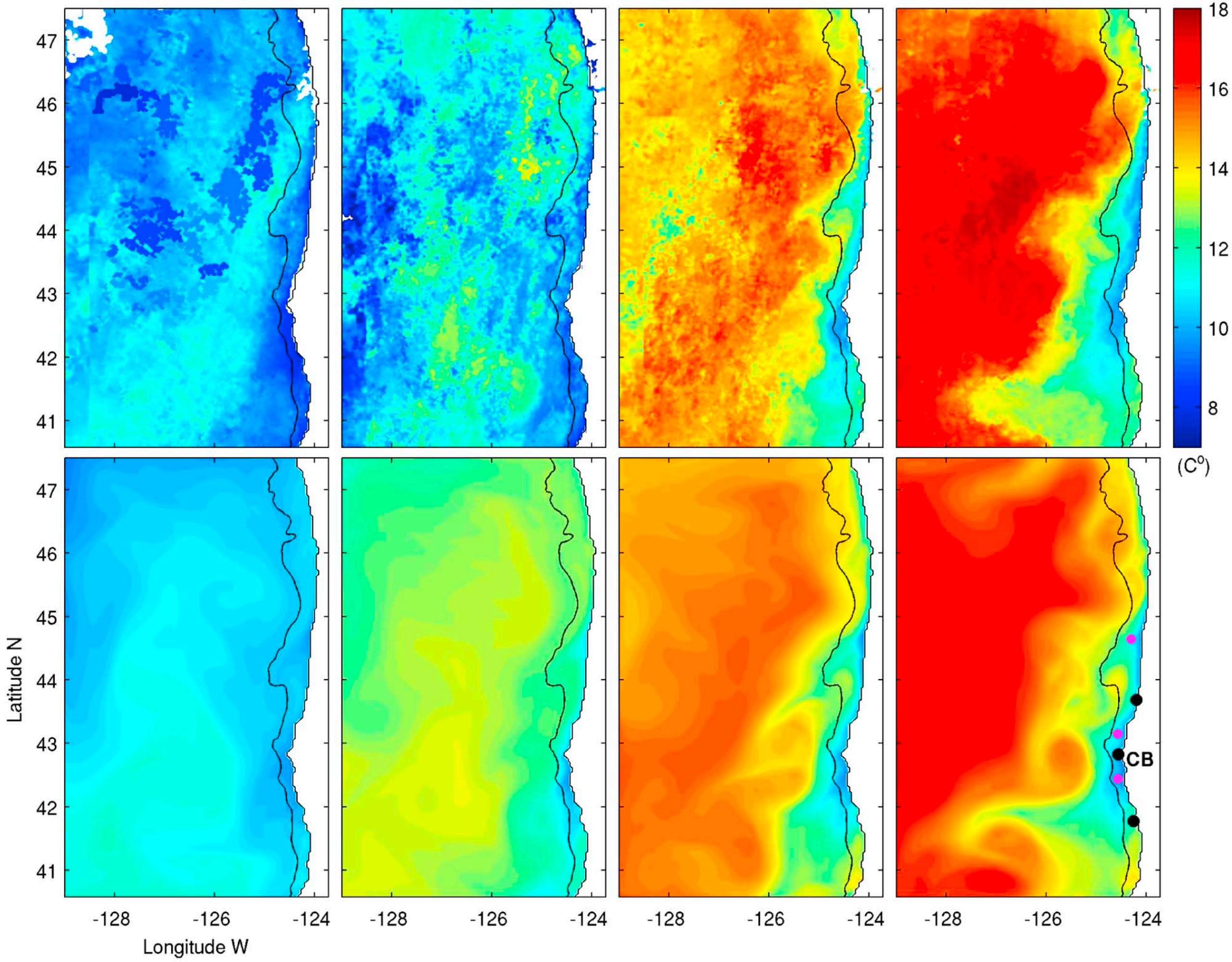

18
16
14
12
10
8
(C^0)
47
46
45
44
43
42
41
Latitude N
-128
-126
-124
Longitude W
CB

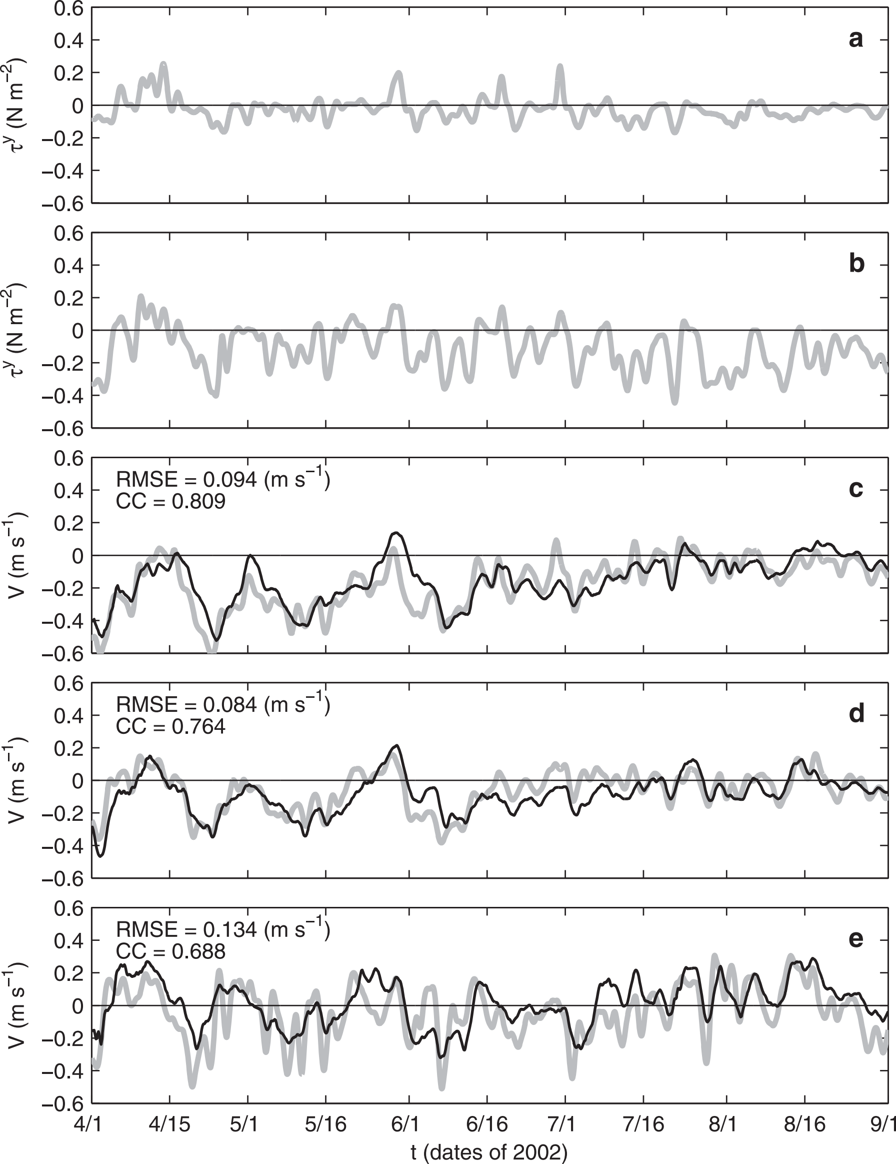

a
b
RMSE = 0.094 (m s^{-1})
CC = 0.809
c
RMSE = 0.084 (m s^{-1})
CC = 0.764
d
RMSE = 0.134 (m s^{-1})
CC = 0.688
e
τ^y (N m^{-2})
V (m s^{-1})
0.6
0.4
0.2
0
−0.2
−0.4
−0.6
4/1
4/15
5/1
5/16
6/1
6/16
7/1
7/16
8/1
8/16
9/1
t (dates of 2002)

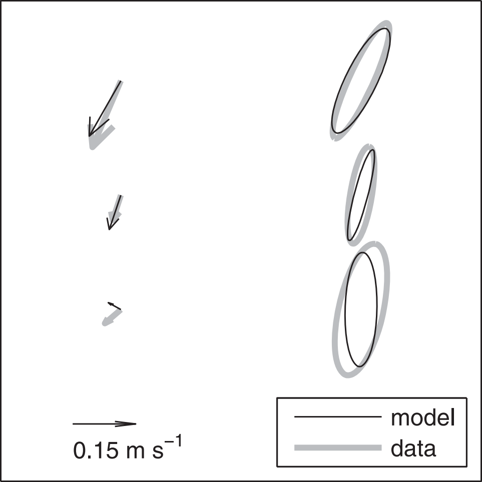
model
data
0.15 m s^{-1}

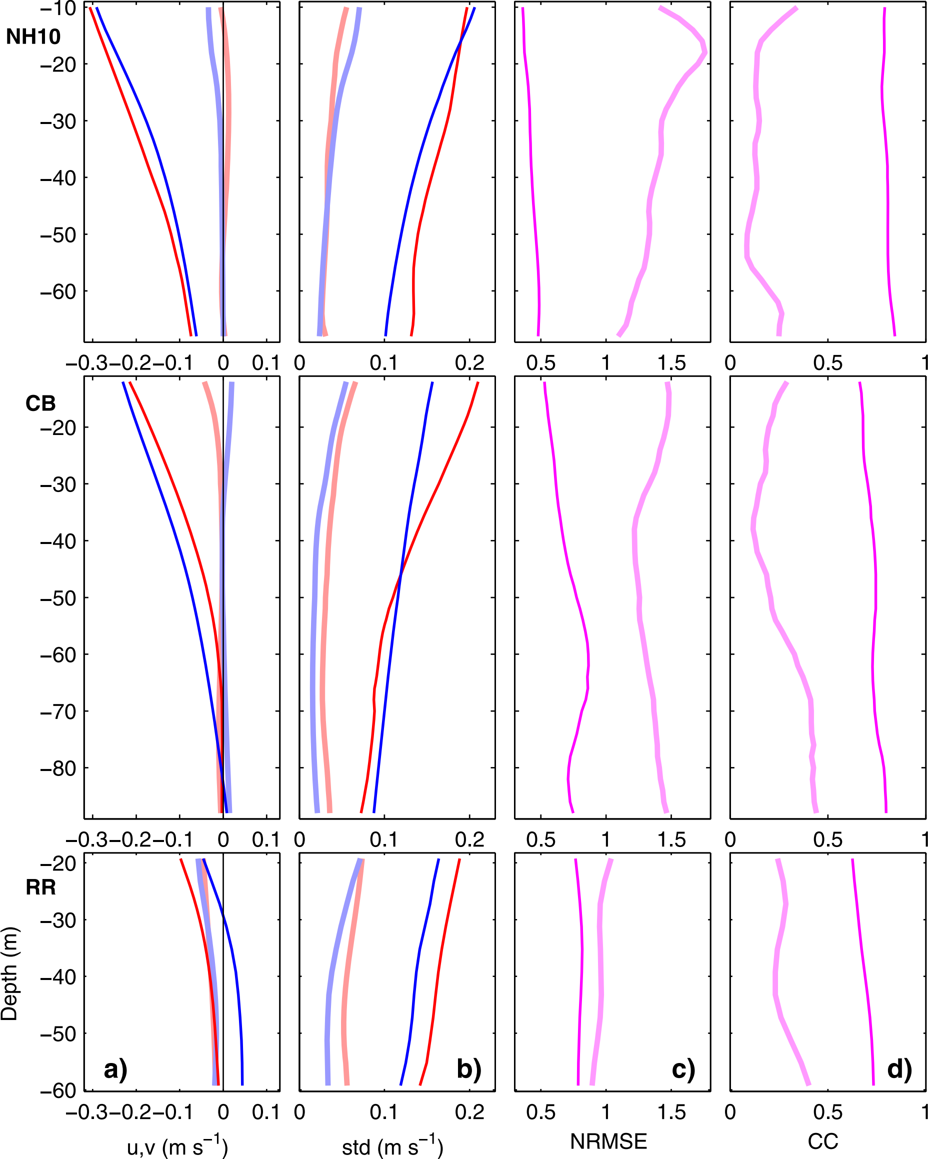

NH10
CB
RR
Depth (m)
a)
b)
c)
d)
u,v (m s^{-1})
std (m s^{-1})
NRMSE
CC

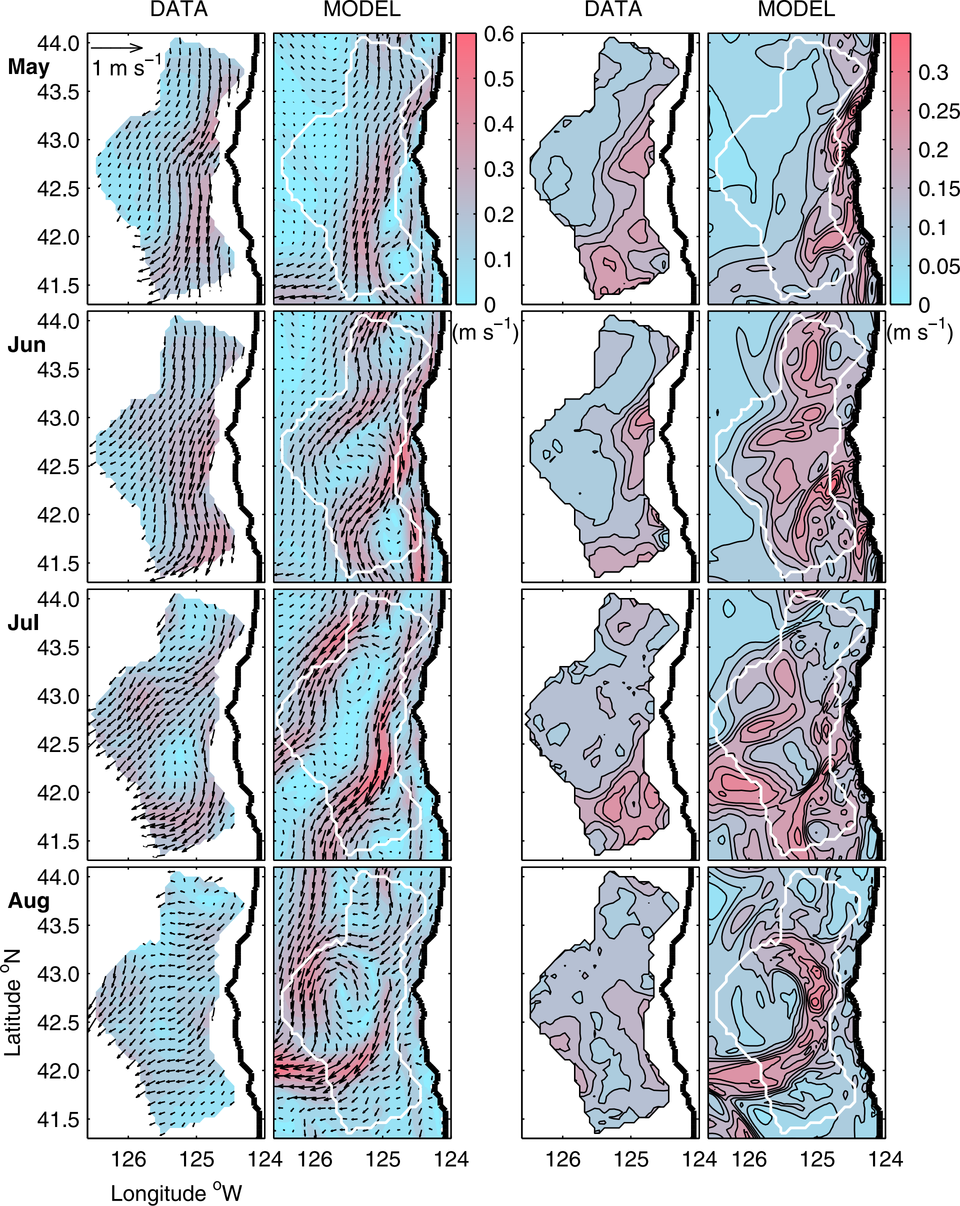

DATA
MODEL
DATA
MODEL
May
Jun
Jul
Aug
1 m s^{-1}
44.0
43.5
43.0
42.5
42.0
41.5
0.6
0.5
0.4
0.3
0.2
0.1
0
(m s^{-1})
0.3
0.25
0.2
0.15
0.1
0.05
0
(m s^{-1})
126
125
124
Latitude ^{o}N
Longitude ^{o}W

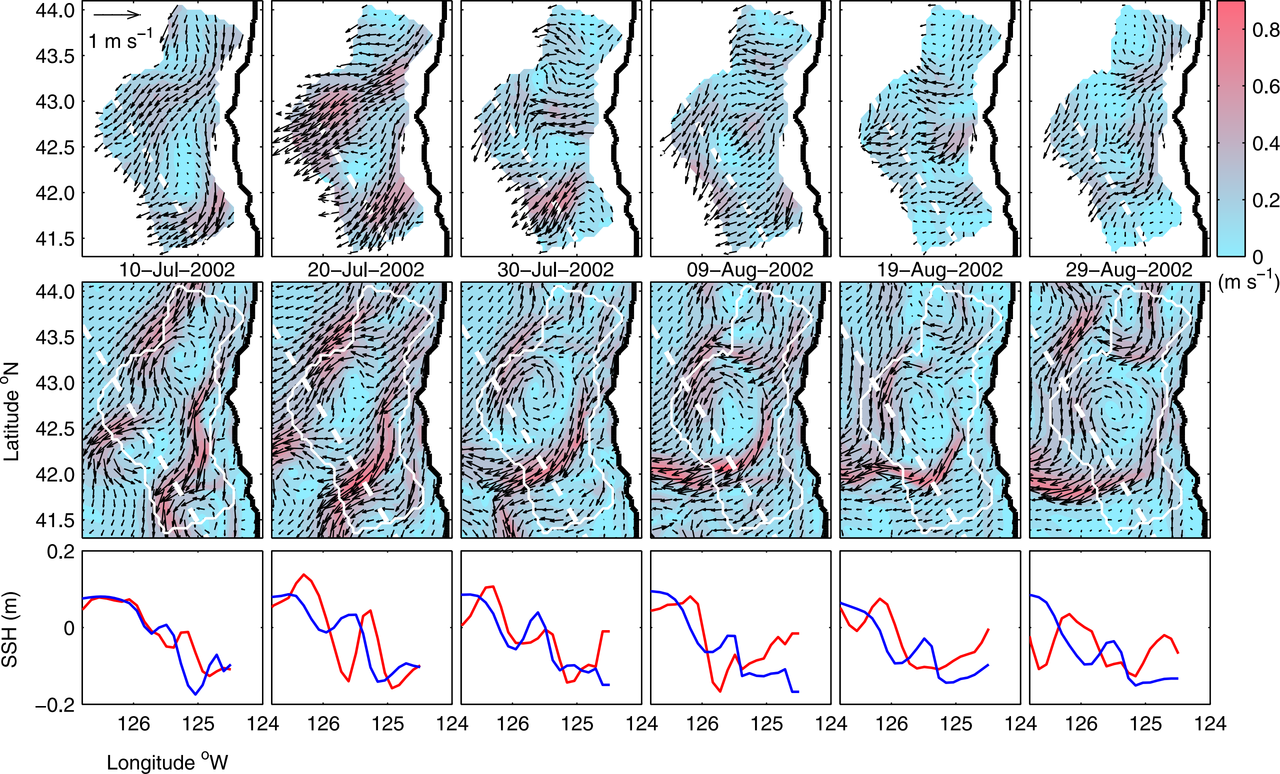

1 m s^{-1}
10–Jul–2002
20–Jul–2002
30–Jul–2002
09–Aug–2002
19–Aug–2002
29–Aug–2002
(m s^{-1})
0
0.2
0.4
0.6
0.8
Latitude °N
44.0
43.5
43.0
42.5
42.0
41.5
SSH (m)
0.2
0
−0.2
126
125
124
Longitude °W

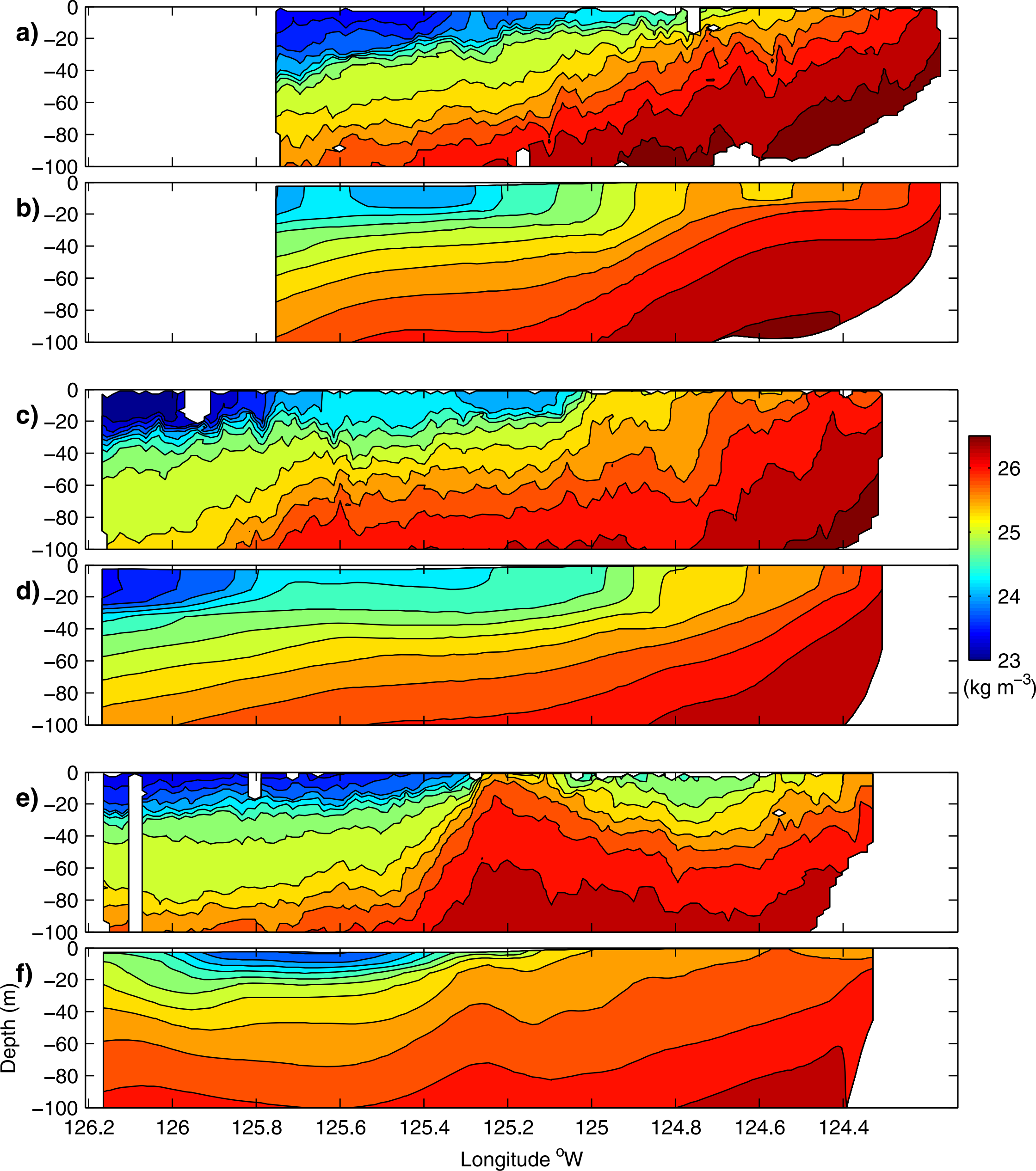

a)
b)
c)
d)
e)
f)
0
−20
−40
−60
−80
−100
Depth (m)
126.2
126
125.8
125.6
125.4
125.2
125
124.8
124.6
124.4
Longitude ^{o}W
26
25
24
23
(kg m^{-3})

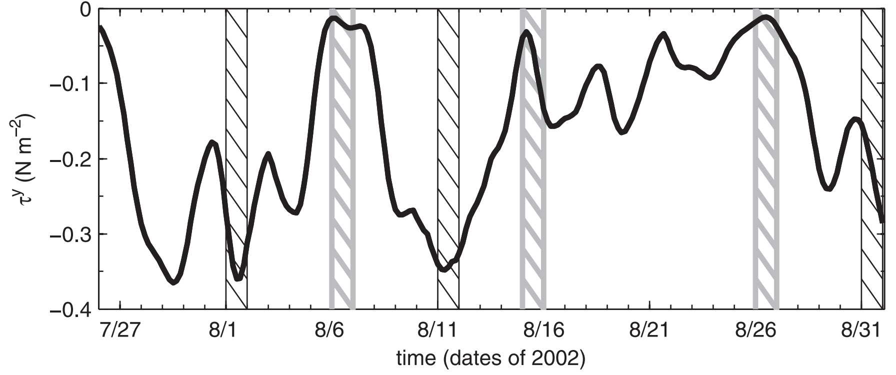

0
−0.1
−0.2
−0.3
−0.4
τ^y (N m^−2)
7/27
8/1
8/6
8/11
8/16
8/21
8/26
8/31
time (dates of 2002)

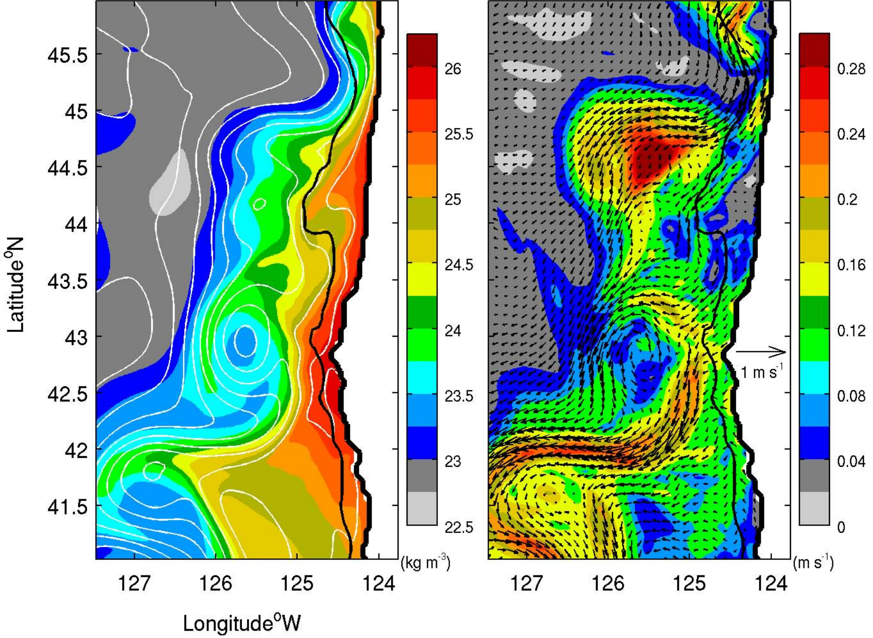

Latitude°N
45.5
45
44.5
44
43.5
43
42.5
42
41.5
127
126
125
124
Longitude°W
26
25.5
25
24.5
24
23.5
23
22.5
(kg m-3)
1 m s-1
0.28
0.24
0.2
0.16
0.12
0.08
0.04
0
(m s-1)

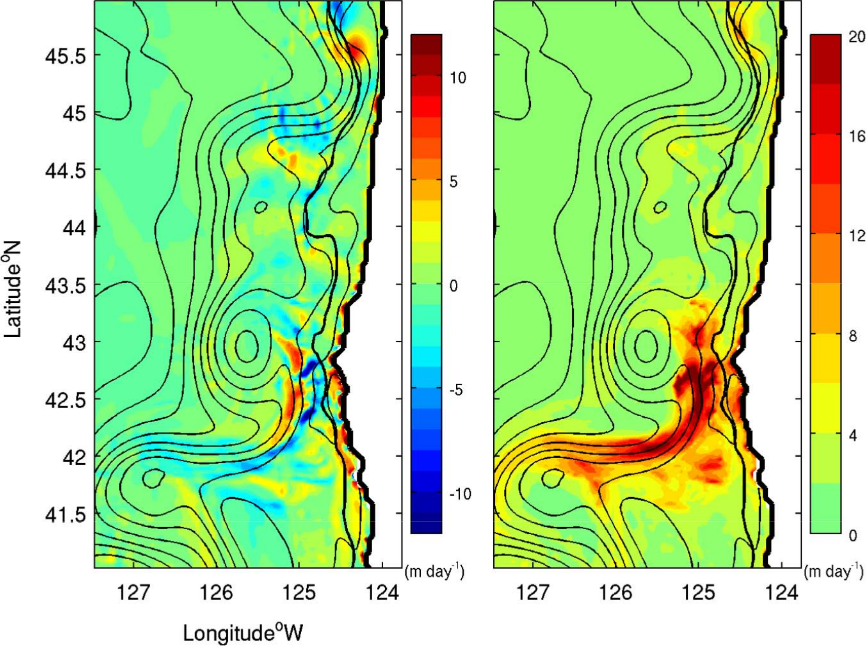

45.5
45
44.5
44
43.5
43
42.5
42
41.5
Latitude°N
127
126
125
124
Longitude°W
10
5
0
-5
-10
(m day-1)
20
16
12
8
4
0
(m day-1)

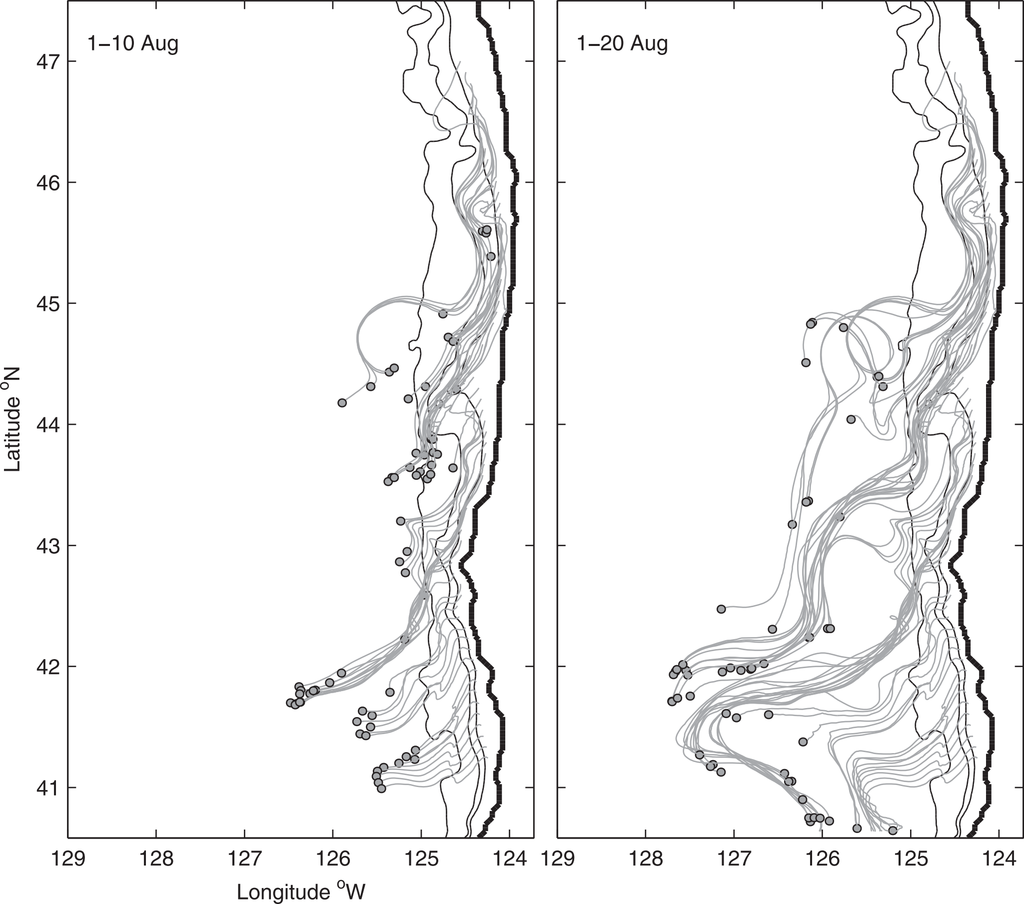
1–10 Aug
1–20 Aug
Latitude °N
Longitude °W
47
46
45
44
43
42
41
129
128
127
126
125
124

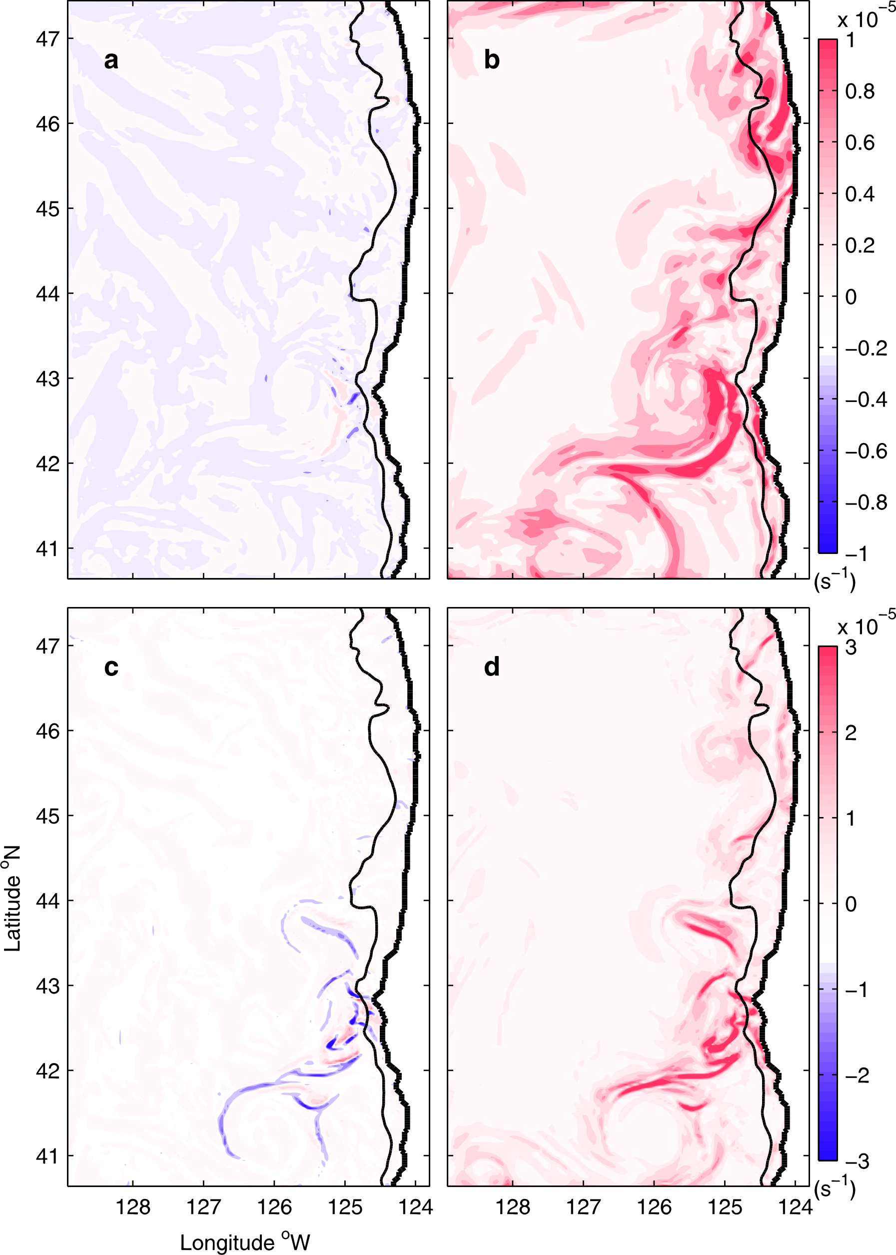

a
b
c
d
47
46
45
44
43
42
41
128
127
126
125
124
Latitude °N
Longitude °W
x 10^-5
1
0.8
0.6
0.4
0.2
0
−0.2
−0.4
−0.6
−0.8
−1
(s^-1)
3
2
−2
−3

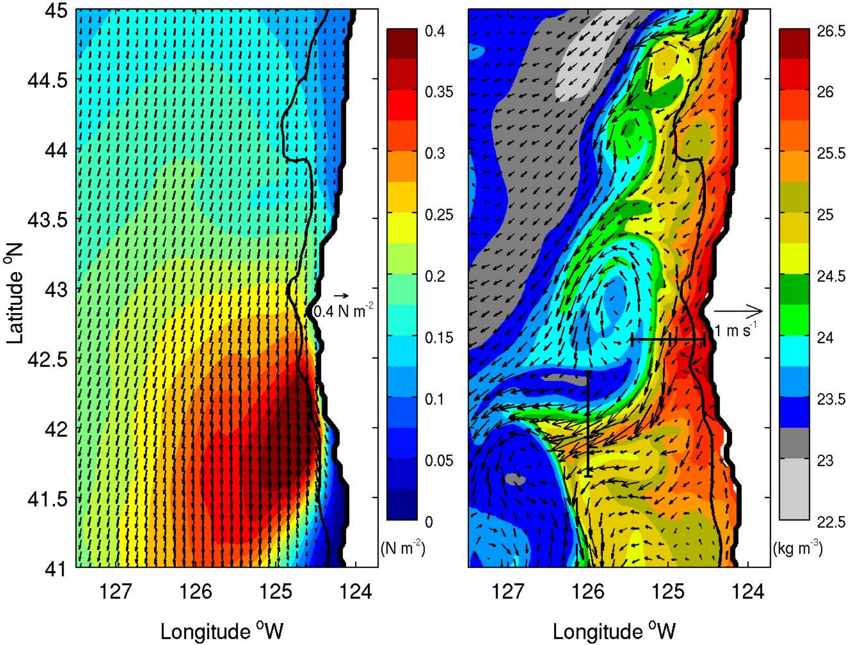

Latitude °N
45
44.5
44
43.5
43
42.5
42
41.5
41
127
126
125
124
Longitude °W
0.4 N m^{-2}
0.4
0.35
0.3
0.25
0.2
0.15
0.1
0.05
0
(N m^{-2})
1 m s^{-1}
26.5
26
25.5
25
24.5
24
23.5
23
22.5
(kg m^{-3})

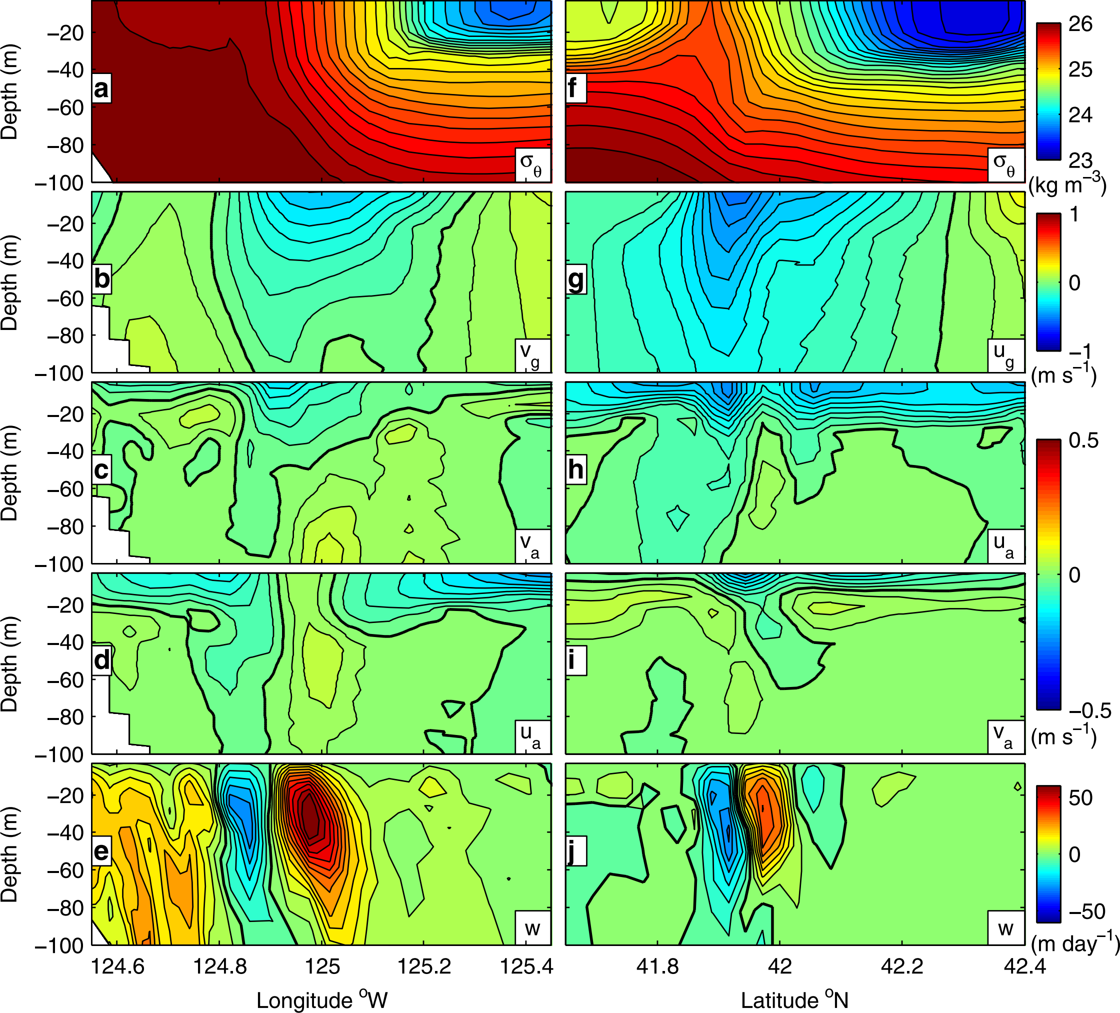

a
b
c
d
e
f
g
h
i
j
σθ
vg
va
ua
w
ug
Depth (m)
Longitude °W
Latitude °N
(kg m−3)
(m s−1)
(m day−1)

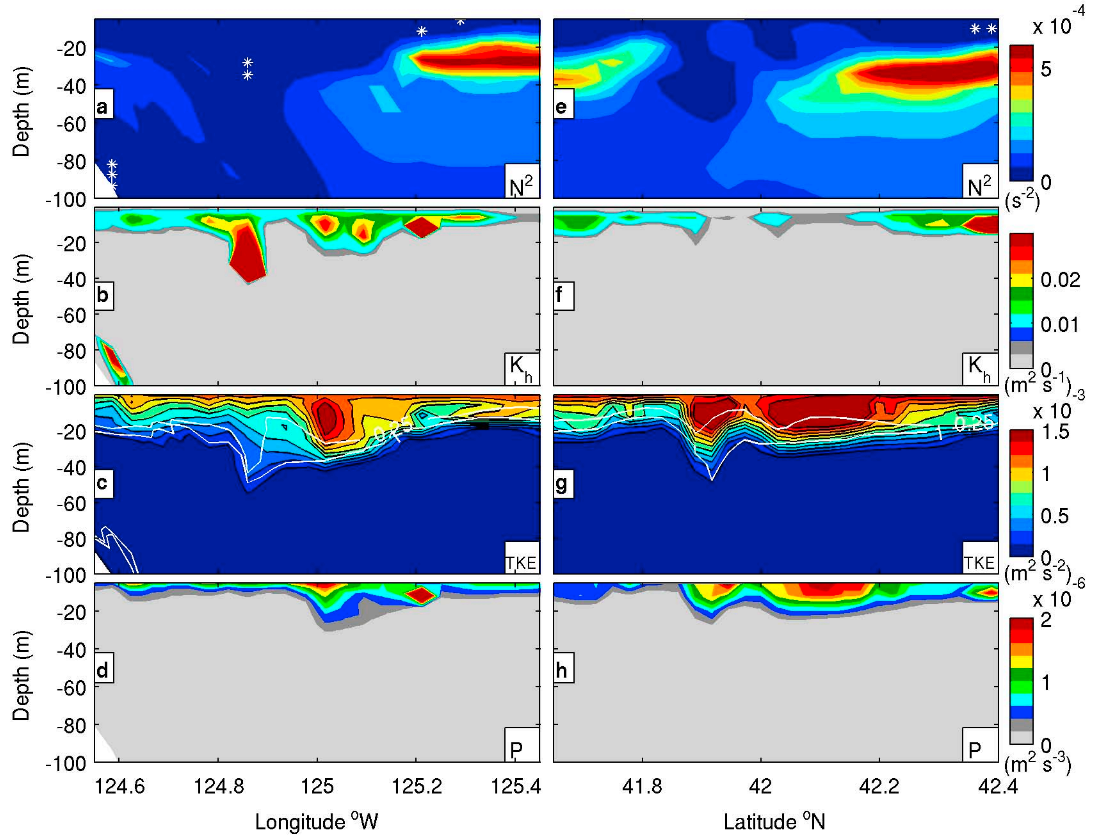

a
b
c
d
e
f
g
h
N^2
K_h
TKE
P
Depth (m)
-20
-40
-60
-80
-100
0.25
x 10^-4
5
0
(s^{-2})
0.02
0.01
0
(m^2 s^{-1})
x 10^-3
1.5
1
0.5
0
(m^2 s^{-2})
x 10^-6
2
1
0
(m^2 s^{-3})
124.6
124.8
125
125.2
125.4
Longitude °W
41.8
42
42.2
42.4
Latitude °N

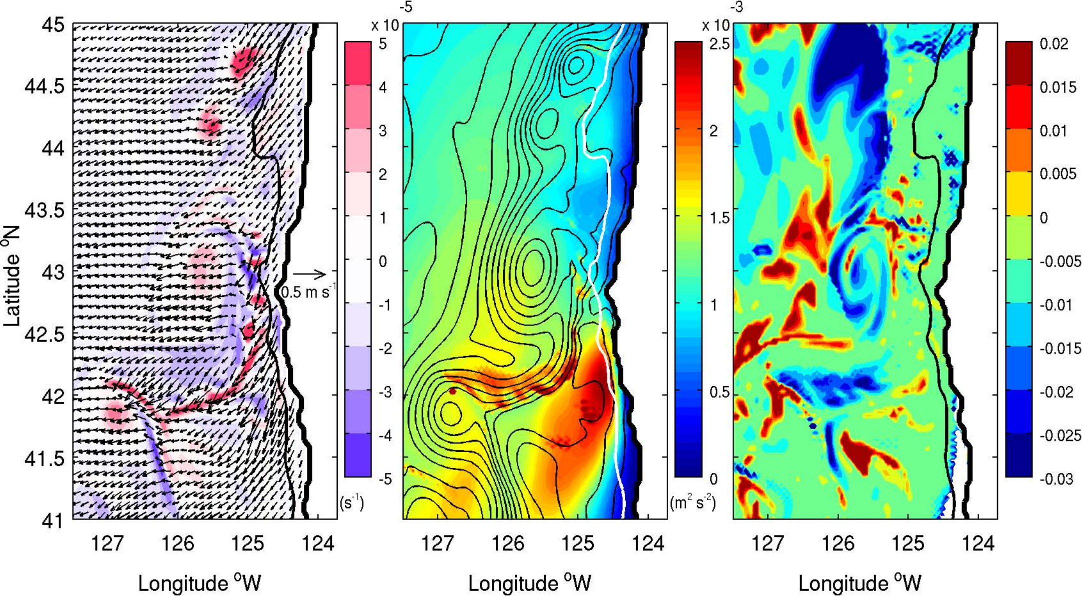

Latitude °N
45
44.5
44
43.5
43
42.5
42
41.5
41
127
126
125
124
Longitude °W
0.5 m s⁻¹
5
4
3
2
1
0
-1
-2
-3
-4
-5
(s⁻¹)
x 10⁻⁵
2.5
2
1.5
1
0.5
0
(m² s⁻²)
x 10⁻³
0.02
0.015
0.01
0.005
0
-0.005
-0.01
-0.015
-0.02
-0.025
-0.03

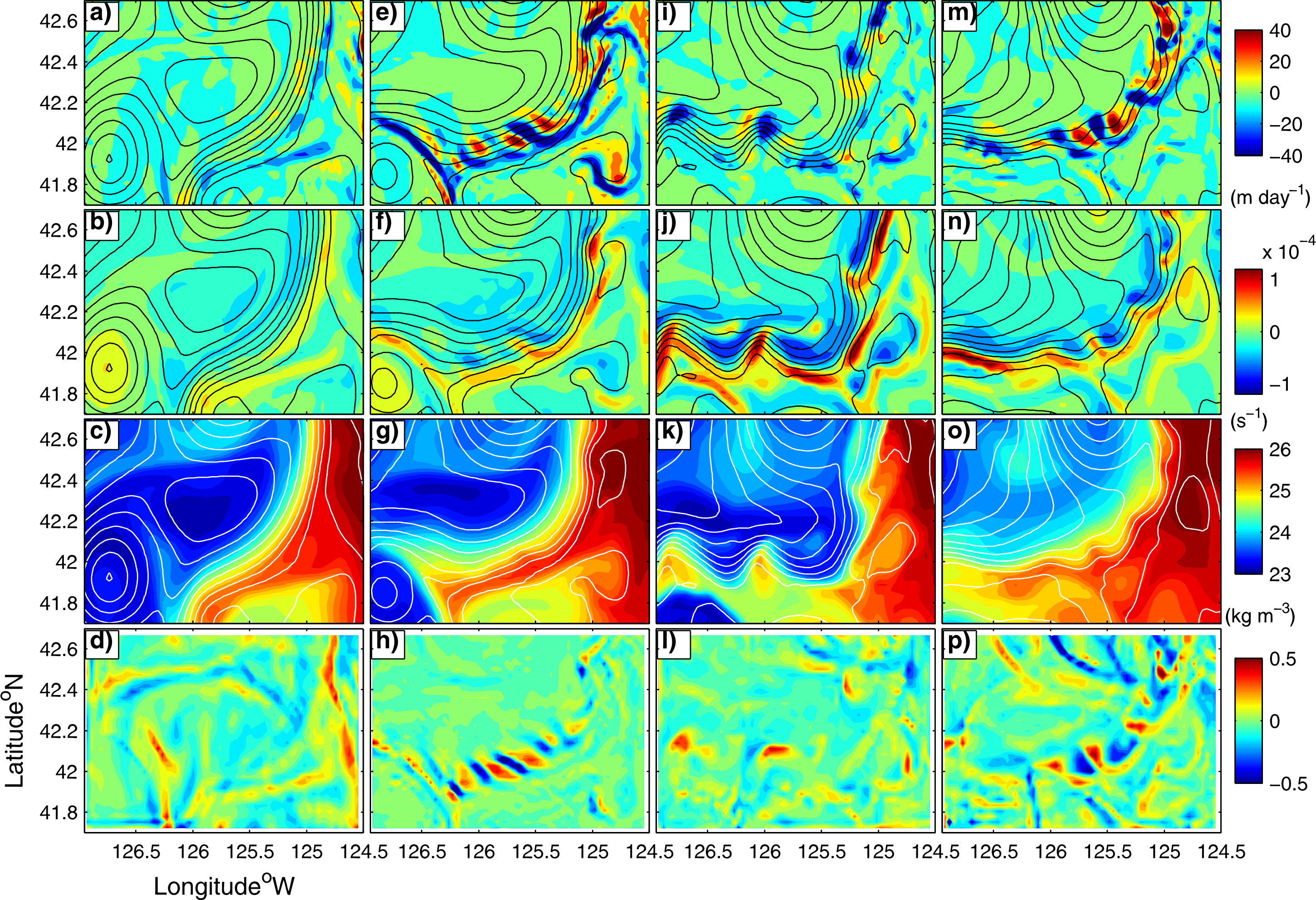

a)
b)
c)
d)
e)
f)
g)
h)
i)
j)
k)
l)
m)
n)
o)
p)
42.6
42.4
42.2
42
41.8
126.5
126
125.5
125
124.5
Longitude°W
Latitude°N
40
20
0
−20
−40
(m day−1)
x 10−4
1
0
−1
(s−1)
26
25
24
23
(kg m−3)
0.5
0
−0.5

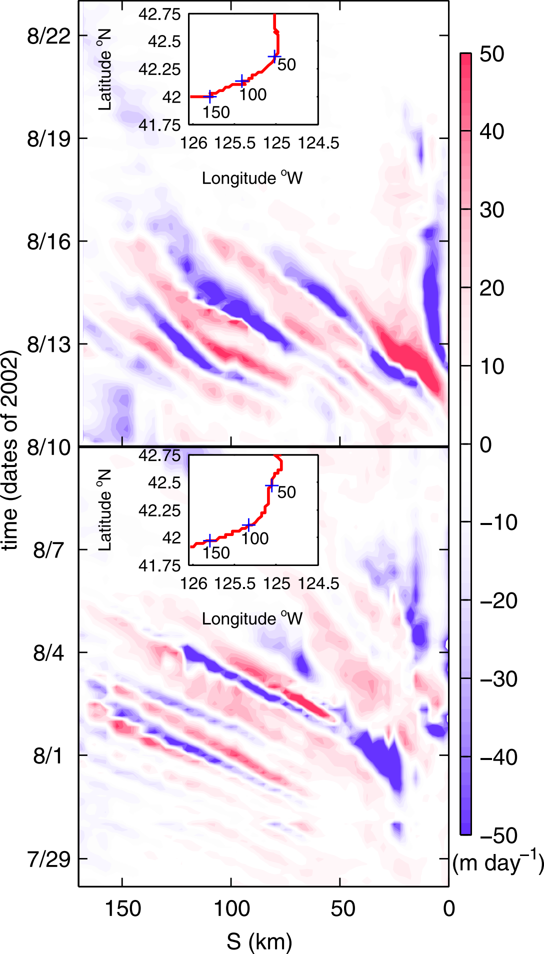

time (dates of 2002)
8/22
8/19
8/16
8/13
8/10
8/7
8/4
8/1
7/29
S (km)
150
100
50
0
Latitude °N
Longitude °W
42.75
42.5
42.25
42
41.75
126
125.5
125
124.5
50
100
150
50
40
30
20
10
0
−10
−20
−30
−40
−50
(m day^{-1})

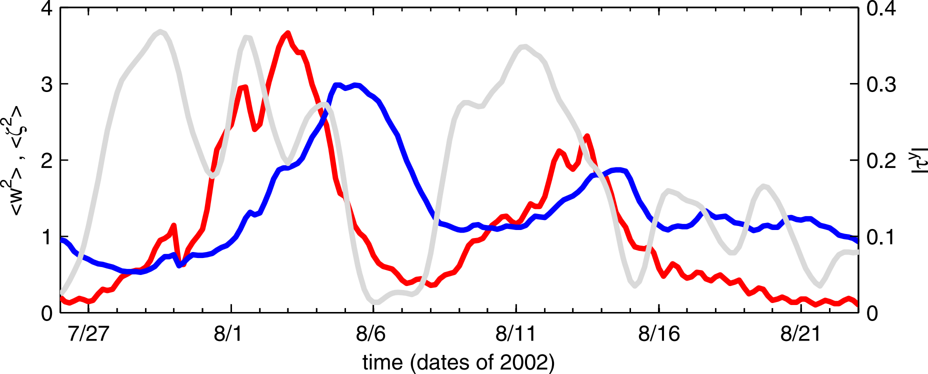

4
3
2
1
0
0.4
0.3
0.2
0.1
0
<w2> , <ζ2>
|τy|
7/27
8/1
8/6
8/11
8/16
8/21
time (dates of 2002)

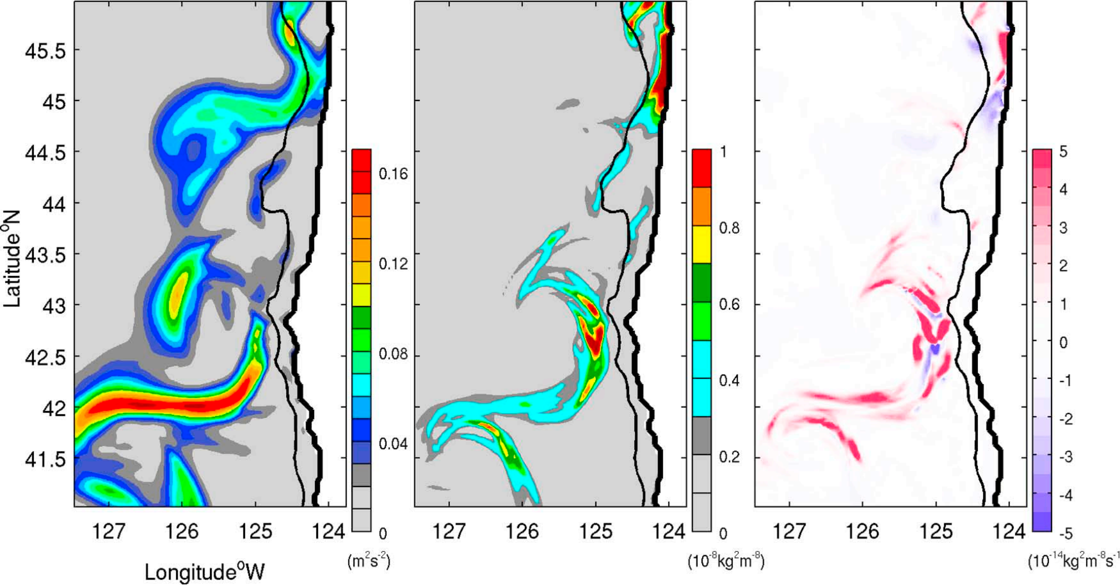

Latitude°N
45.5
45
44.5
44
43.5
43
42.5
42
41.5
127
126
125
124
Longitude°W
0.16
0.12
0.08
0.04
0
(m2s-2)
1
0.8
0.6
0.4
0.2
0
(10-8kg2m-8)
5
4
3
2
1
0
-1
-2
-3
-4
-5
(10-14kg2m-8s-1

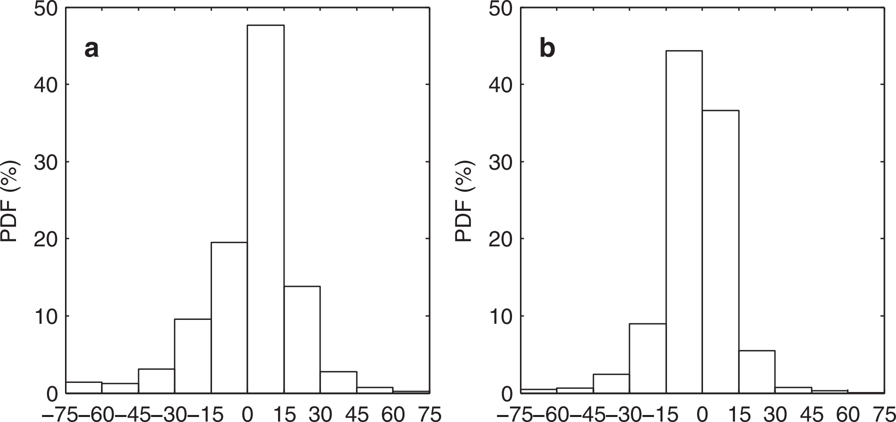
a
b
PDF (%)
PDF (%)
0
10
20
30
40
50
−75 −60 −45 −30 −15 0 15 30 45 60 75